Case Studies in Thermal Engineering 59 (2024) 104535

Contents lists available at ScienceDirect

Case Studies in Thermal Engineering

journal homepage: www.elsevier.com/locate/csite

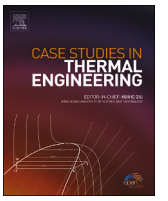

Experimental and simulated evaluation of inverse model for shallow underground thermal storage

Fabian Eze [a, b], Wang-je Lee [b], Young sub An [b], Hongjin Joo [b], Kyoung-ho Lee [b, *], Julius Ogola [c], Julius Mwabora [a]

[a] Department of Physics, University of Nairobi, 30197 – 00100, Nairobi, Kenya
[b] Renewable Energy System Laboratory, Korea Institute of Energy Research, 152, Gajeong-ro, Yuseong-gu, Daejeon, 34129, Republic of Korea
[c] Department of Mechanical and Manufacturing Engineering, University of Nairobi, 30197 – 00100, Nairobi, Kenya

HIGHLIGHTS

- Experimental setup for shallow underground thermal storage was conducted.
- Detailed TRNSYS and inverse grey-box models were developed.
- Inverse model training and testing were carried out using measured data.
- Inverse model was evaluated with the calibrated TRNSYS model for various conditions.

ARTICLE INFO

Keywords:
Shallow underground thermal storage
Inverse grey-box model
Model calibration
Experimental data
Simulated data
Training and testing

ABSTRACT

This study employs an inverse grey-box (IGB) modeling approach, which combines measured data and the physics of systems to predict the performance of shallow underground thermal energy storage (UTES) with top and side insulation. A simplified IGB model of the shallow UTES was developed using thermal network analysis. Experimental studies were conducted for shallow vertical and horizontal UTES configurations. Detailed models representing the field experiments were developed using the TRNSYS simulation tool and calibrated with the measured data from the experimental setup. The 4 Resistance 2 Capacitance (4R2C) IGB model was trained and tested in MATLAB using field experimental data and the data from the calibrated TRNSYS model. In comparing experimental data with the TRNSYS model for UTES, the prediction of outlet water temperature showed good agreement, with root mean square error (RMSE) and coefficient of variation of RMSE (CVRMSE) values of 0.94 °C and 3.16 % for vertical, and 0.99 °C and 2.97 % for horizontal configurations. The IGB model also aligned well with the experimental data, showing CVRMSE of 7.91 % and 3.17 % for vertical and horizontal systems, respectively. Sensitivity analysis revealed that model performance improves with longer training durations and closer testing times to training periods. However, a convergence point of 20 weeks of training data was achieved for making long-term performance predictions.

* Corresponding author.
E-mail address: khlee@kier.re.kr (K.-h. Lee).

https://doi.org/10.1016/j.csite.2024.104535
Received 5 December 2023; Received in revised form 27 April 2024; Accepted 10 May 2024
Available online 11 May 2024

Parameters and abbreviations

Symbols	Description (unit)
A_f	Heat transfer surface are of the pipe (m^2)
C_g	Volumetric heat capacitance of the grouting material (kJ/K)
c_{pw}	Specific heat capacity of water (kJ/kg·K)
h_f	Fluid convective heat transfer coefficient (kJ/hr·m^2·K)
N	Number of boreholes
$\dot{m}_w$	Mass flow rate of working fluid (kg/hr)
$\dot{Q}_w$	Heat transfer rate (kJ/hr)
T_g	Temperature at the grouting node (^{o}C)
T_G	The effective temperature of far-field soil outside the insulation (^{o}C)
T_{soil}	The soil (ground) temperature of the borehole storage volume (^{o}C)
$\overline{T}_w$	Average water temperature (^{o}C)
T_{in}	Inlet water temperature to the borehole (^{o}C)
T_{out}	Outlet water temperature from the borehole (^{o}C)
Thermal Resistances	
R_{wg}	Water to grout thermal resistance (K·hr/kJ)
R_{gs}	Grout to soil thermal resistance (K·hr/kJ)
R_{as}	Ambient to soil thermal resistance (K·hr/kJ)
R_{sG}	Thermal resistance between T_G and the T_{soil} (K·hr/kJ)
Soil	
C_{soil}	Thermal capacitance of soil (kJ/K)
c_{ps}	Specific heat capacity of soil (kJ/kg·K)
ρ_s	Density of the soil (kg/m^3)
V_s	Volume of the borehole (m^3)
Pipe	
L	Effective length of the borehole pipe (m)
r_{p1}	Inner radius of the pipe (m)
r_{p2}	Outer radius of the pipe (m)
r_b	Borehole Radius (m)
Other borehole parameters	
A_s	Surface area of borehole (m^2)
$A_{surf,ins}$	Soil area above top insulation slab (m^2)
A_{ins}	Area of insulation slab (m^2)
$A_{ins,s}$	Soil area below top insulation slab (m^2)
$A_{s,ins}$	Area of soil to side (vertical) insulation (m^2)
$A_{ins,G}$	Area of side (vertical) insulation to far-field (m^2)
$h_{\_air}$	Convective heat transfer coefficient of air (kJ/hr· m^2·K)
c_{pg}	Heat capacity of the grouting material (kJ/kg·K)
ρ_g	Density of the grouting material (kg/m^3)
V_g	The volume of the grouting material (m^3)
α	A dimensionless factor
k_p	Thermal conductivity of pipe (kJ/hr·m·K)
k_g	Thermal conductivity of grout material (kJ/hr·m·K)
k_{ins}	Thermal conductivity of insulating material (kJ/hr·m·K)
k_s	Thermal conductivity of soil (kJ/hr·m·K)
$L_{surf,ins}$	Distance above the top insulation slab (m)
$L_{ins,s}$	Distance below the top insulation slab (m)
L_{ins}	Insulation thickness (m)
$L_{s,ins}$	Distance from soil to side insulation slab (m)
$L_{ins,G}$	Distance from side insulation slab to far-field (m)
l_b	Effective length of the heat conduction path (m)
r_g	Radius of grout (m)
Abbreviations	
ANN	Artificial Neural Network

(*continued on next page*)

(*continued*)

Symbols	Description (unit)
ASHP	Air Source Heat Pump
CFD	Computational Fluid Dynamics
CVRMSE	Coefficient of Variation of Root Mean Square Error
GenOpt	Generic Optimization Program developed by NREL
HVAC	Heating, Ventilation, and Air-Conditioning
IGB	Inverse grey-box
MPC	Model Predictive Control
NRMSE	Normalized Root Mean Square Error
PCM	Phase Change Material
PSO	Particle Swarm Optimization
PV/PVT	Photovoltaic/Photovoltaic Thermal
RMSE	Root Mean Square Error
SAGSHP	Solar-assisted ground-sourced heat pump
SSE	Sum of square Errors
TES	Thermal Energy Storage
TRNSYS	Transient System Simulation Program developed by University of Wisconsin
TRRA	Trust-reflective algorithm
UTES	Underground Thermal Energy Storage

1. Introduction

Building energy consumption is increasing exponentially due to the economic development in different parts of the world. About 40 % of the global energy consumption is attributed to the energy use in buildings, and approximately 60 % of this is linked to heating and cooling alone [1]. Over the years, the use of fossil fuels has been employed to meet this energy demand; however, they emit greenhouse gases into the atmosphere, which results in climate change and consequent global warming. There is also a concern about their depletion over time, hence necessitating the use of renewable energy as an alternative energy source [2]. Moreover, renewable energy sources such as solar energy suffer some retarding challenges in the areas of harnessing and storage. This issue has led to a significant amount of energy waste in the application of solar photovoltaic (PV) and solar thermal, including photovoltaic thermal (PVT), since solar energy is time-dependent. Thermal energy storage (TES), which is an energy storage in the form of heat for future use, has proven to be efficient in mitigating the wastes [3]. TES can be accomplished by the use of conventional insulated tanks, vacuum insulated tanks, phase change materials (PCM), and Underground thermal energy storage (UTES) with or without auxiliary energy sources [4]. It can be diurnal or seasonal (mid-term and long-term), depending on the intended application [5]. The diurnal TES are primarily designed to store thermal energy during the day when solar energy is abundant and release it during periods of high demand, such as nighttime [6]. However, seasonal TES involves a design that allows for inter-seasonal storage and consumption of thermal energy to bridge the gap between seasonal variation in energy demand and supply [7,8]. The latter is the concept presented in the current study. In general, the heat stored using any of the TES methods is used for heating and cooling applications in both residential and commercial buildings on integration with models such as a heat pump. Among the methods of TES, UTES is the most promising since it has great potential for mid-term thermal storage and is considered the cheapest, along with its market value previously forecasted to increase yearly by 13.1 % until 2020 [9]. UTES is similar to ground heat exchangers (GHE); however, it is important to note that while both UTES and GHE utilize the thermal properties of the ground for heating and cooling purposes, with the help of a heat pump, they serve different purposes and are designed differently. UTES focuses mainly on the mid-term storage of thermal energy in the ground itself, aquifers, rocks, or soil layers for later use, while GHE is used for *direct* heat exchange with the ground to provide heating or cooling to buildings or systems [10]. The UTES system operates by injecting heat into the ground when heating or cooling is not needed, and extracting the heat from the ground when heating or cooling is required. This process can also be used for domestic hot water (DHW) purposes and is considered the most promising thermal energy storage technique due to its consistent temperature source. The ground, at certain depths, maintains nearly a constant temperature all year round, enabling the ground-source heat pump system to perform efficiently in different seasons of the year, unlike conventional systems such as the air source heat pumps (ASHP). However, the higher the depth, the more expensive the system installation and the overall costs, making shallow UTES a more reliable option [11]. Even in some research such as [12], ground temperature source is leveraged for the design of an underground thermal battery consisting of a tank incorporated with PCM for heat enhancement and at depth of about 6 m.

1.1. Underground thermal energy storage

In general, UTES systems are classified into vertical and horizontal types based on their configurations for seasonal space heating and cooling applications in both commercial and residential buildings [13,14]. The configurations are such that pipes of different thermal properties are buried in layers at different depths, usually between 10 and 150 m below the ground for conventional systems. Water at a given temperature is supplied to the pipe inlet at a flow rate necessary to initiate a larger temperature difference between the inlet and outlet for a higher fluid-to-ground heat transfer rate. The UTES with higher depths constitute high installation costs with little improvement in the system's efficiency; therefore, to reduce the cost of installation and improve efficiency, numerical and experimental analysis of shallow types with depths between 1 and 4 m have become of great interest. For instance, Kim et al. [11] manufactured and tested a modular UTES buried at a depth of 4 m below the ground surface that can be employed in mid-term thermal storage and applications. The test results showed a heat transfer rate of 78.98 % and 88.83 % during heat storage and heat release, re-

spectively, and an increase in temperature of 4.4 °C during heat and 1.2 °C drop during heat release. Naranjo-Mendoza et al. [9] experimentally investigated a solar-assisted ground-source heat pump (SAGSHP) system incorporated with shallow UTES in residential building applications. The system contains 16 boreholes with a 1.5 m distance between the adjacent boreholes. The UTES was sited outside the foundation of the house and insulated with polyisocyanurate of 20 cm on top and 10 cm by the sides, with 0.3 mm polythene cover for water penetration prevention. Working fluids for solar and ground loop is both glycol (30 %) and water. 3 kW heat pump and 200 L DHW tank were used. The study established that thermal energy can be stored in the earth energy bank (EEB) during the summer and used for domestic purposes during the winter. Energy balance showed that about 18 % and 82 % of the energy stored are from geothermal and solar PVT, respectively. The heat pump uses 54 % of the energy directly while 46 % is stored in the EEB and 6 % thermal losses. The study by Başer and McCartney [15] explored the performance of underground TES system installed in San Diego, California to evaluate its advantages in a vadose zone. Simulation and experimental result indicated excellent match showing that coupled heat transfer and water flow are important consideration in soil borehole TES system installed in a vadose zone. Various numerical studies have been carried out as well for performance investigation of UTES. Gultekin et al. [16] examined the effects of various parameters, which include a number of U-tube spacing, working duration, and thermal conductivity, on the thermal performance of a UTES system regarding their heat transfer rates using a 2D finite element method. The thermal energy interaction between boreholes increases as the number of boreholes increases. This implies that the increase in the number of boreholes increases interactions over time, resulting in higher thermal loss. Gultekin et al. also reported a decrease in the thermal losses as the distance between each borehole and the others increased. Numerical modeling of a solar system that utilizes the Borehole thermal Energy Storage was carried out by Abualqumboz and Rodley [17]. Although the study made several assumptions for simplification, the results of the numerical modeling match other results existing in the literature. However, an experimental approach is required for further validation.

1.2. Inverse model

Numerical analysis of UTES is one of the ways to ascertain the performance of the system before experimentation; however, modeling and evaluation of the systems appear to be complicated for optimal and easy use due to the uncertainties in the accuracy of their driving parameters. Model development suffers some setbacks as a result of the limitation in their abilities to identify the best physical parameters. Based on the ASHRAE handbook [18], system modeling is classified into forward and inverse models. Forward modeling deals with a physical description of the system and is applied in the design of HVAC systems, while the inverse model involves the representation of the system driving forces using their physical properties and observing the system behavior with the use of measured data [19]. The models for thermal analysis can be classified into the white-box (WB), black-box (BB), and inverse grey-box (IGB) models. The white-box model uses only the physical representation of the system to predict and evaluate system performance. Thermal energy systems analyzed by the use of energy simulation software such as TRNSYS [20] and EnergyPlus [21] belong to this model category [1]. Its limitation is that it uses many parameters that are either known or require a lot of time and resources to measure hence is not cost-effective. In addition, it must be validated with measured data from an actual system. The research carried out by Maestre et al. [22,23], belong to this category. The study in Ref. [12], developed a simplified one-dimensional R–C model combined with rapid and lengthy time-step g-functions for a single U-tube UTES to simulate the heat transfer profile of the system. The model was later updated to a two-dimensional model in Ref. [22]. The results of the simulation were validated using CFD reference model from ANSYS CFX and the results showed good agreement with the RMSE for water outlet temperatures less than 1 °C and 0.15 °C for the one-dimensional and two-dimensional models respectively. Tu et al. [24] developed a revised R–C model for single U-tube UTES that takes into consideration the freezing conditions in the ground. The model was validated using field data and the result indicated concurrency with a properly set system parameters. It was shown that under freezing conditions, the model can maintain heat transfer rate between 75 W/m to 80 W/m in a three-month period. One non-dimensional mathematical model for predicting the performance of a low-depth modular ground heat exchanger (GHX) for small occupancy building was developed by Kim and Nam [25] using finite element sun-surface FLOW (FESFLOW) for simulation. The model considered a 40 mm pipe grouted with concrete 2 m below the earth surface. The comparison of the predictive and numerical models showed good agreement when validated by ASHRAE recommended RMSE method. However, 8 h experimental results showed disagreement with the numerical and predictive model giving difference of 10.64 % and 18.08 % respectively at low-depth of 2 m although the heat exchange rate agreed to both predictive model and numerical analysis. This discrepancy was attributed to the weather variations and operational conditions.

The black-box model, on the other hand, makes use of the input and output data for the description of the system through the application of regression analysis, transfer function, or artificial neural networks (ANN). The use of a black box model for the evaluation and prediction of thermal systems can yield good results, especially when the prediction of future behavior of such system is of the greatest interest; however, collection of data over a long period of time is required. otherwise, it may not represent the proper physics of the system. In other words, the quantity and quality of the datasets are vital for the system's effectiveness. For more insight into the black-box model, Lee et al. [26] applied model predictive control (MPC) that uses ANN to predict the long-term behavior of building energy system integrated with TES. The authors used about 64 datasets to configure the model while training, verifying, and testing the model with 70 %, 15 %, and 15 % of the dataset, respectively. In the application of thermal energy storage, ANN was utilized by Ren et al. [27] to predict the charging and discharging of Phase Change Material (PCM) and the result proved efficient although it depends on the reliability of the data used for the training. Amarasinghe et al. [28] used ANN based TES for building operating control using the TES, power availability building power requirement forecast, and utility load forecast for the succeeding hour. The result showed that the proposed controller increased the cost savings and minimized wastages.

The inverse grey-box model is a combination of white and black-box models for system prediction and evaluation. It combines the mathematics behind the system comprising the driving physical parameters and measured data. The developed mathematical model is trained with the input-output measured data for the identification of the optimum parameters. This method has proven to be more

efficient in predicting and evaluating system performances since it saves time and cost, increases computational speed, and minimizes uncertainties; however, its application in thermal engineering has been limited. The development of an inverse grey-box model that allows parameter optimization through learning for a nearly accurate forecasting of building energy load was carried out by Braun and Chaturvedi [19]. The model utilizes a transfer function and employs the use of a short time measured data for training while setting optimization parameters to a given lower and upper bounds. The trained model was tested on a different building in a different location and the result showed that short time data is sufficient for model training to predict building HVAC requirements. Liu and Cai [29] used grey-box method to model various servo direct expansion systems and carried out model training with limited measured data based on two-stage training technique that uses parameter impact ranking. The estimated parameters with the limited field data indicated reasonable accuracy when tested on 3-ton variable-speed heat pump. Jeon et al. [1] applied grey-box model for the estimation of building loads and energy demand for optimal predictive control strategy. The authors developed 7R5C model where the parameters are estimated through learning using particle swarm optimization (PSO) technique with and without weather prediction. Result of the learning-based predictive control shows good agreement for both with and without weather prediction having a maximum RMSE of 1.52 ˚C. The effectiveness of white-box, black-box, and grey-box models in system analysis is noteworthy, and researchers have conducted comparative analyses in this area. In the field of software testing, Khan and Khan [30] concluded that the white-box model is particularly suitable for algorithm testing, although it requires expertise and significant resources compared to black-box and grey-box models. Pintelas et al. [31] employed datasets from education, finance, and health to develop a grey-box model that outperformed the other types. Furthermore, a recent critical review conducted by Li et al. [32] explored the application of grey-box models in building modeling and generally found them to be more robust in predicting the performance of thermal energy systems. However, the authors suggested that researchers should broaden their applications beyond energy/load systems to other types of systems.

Existing literature highlights that while shallow Underground thermal energy storage (UTES) systems are a more cost-effective option for heating and cooling applications, they still face challenges related to significant thermal energy loss from the top and sides of their storage volumes, necessitating improvements. Only a few experimental studies have implemented such insulation; however, in the development of the IGB models for shallow UTES, it has not been applied, thereby necessitating the present study. It was also established that the grey-box modeling approach is the most suitable when driving parameters are unknown or difficult and expensive to determine. In addition, the approach enables the prediction of the long-term performance of systems with a short range of training data, provides more reliable results, and reduces uncertainties, unlike other machine learning models, such as the ANN, which require a large range of training data to make long-term performance predictions. However, its application in the modeling and simulation of UTES systems is limited, again calling for further study. To successfully apply the IGB model, measured data from field experiments conducted over either a short or long period must be available. In most previous studies, generated data from white-box models such as ANSYS, COMSOL, FEFFLOW, etc, were utilized rather than data from the actual system. Hence, it is essential to perform a study that simulates the actual systems with provided insulation.

1.3. Objectives and contributions of the study

In this study, experimental studies of shallow UTES for both horizontal and vertical configurations were conducted for use in model calibrations. The experiment contributes to the current knowledge by improving its performance through the prevention of thermal losses by providing 0.2 m thick insulation on the top and sides of the storage volume using polyurethane foam. A similar system was developed in the TRNSYS simulation tool, and the TRNSYS model was calibrated using the measured data. Additionally, a simplified IGB model for shallow UTES was developed using thermal network analysis. This model incorporates the top and side insulations of the UTES systems, as well as the influence of environmental and ground far-field temperatures on the storage volume. To evaluate the performance of the developed 4R2C model, it was calibrated through training and testing processes using both measured data and TRNSYS simulation data. MATLAB was utilized for the training and testing, employing a nonlinear optimization method. Further to this, other models from previous studies were reviewed, and their results were compared with the simplified IGB model. The developed and calibrated models will contribute to the current knowledge by making themselves useful in short and long-term performance prediction of shallow UTES using a short range of training data, where model driving parameters are not known and require significant resources to determine.

2. Methodology

2.1. Model calibration

The performance of predictive models is influenced by their parameters; nonetheless, these parameters are either difficult to determine, costly, or time-consuming, necessitating system model calibration. Model calibration is accomplished through training, verification, and testing. Through calibration, researchers diligently modify the predictive models' output to match their actual behavior [1,33,34], using historical or measured data from the actual system. In this study, the calibration process is as illustrated in Fig. 1. Experimental data collected over a long period of time is split into two sets: a training set and a testing set. Using the training set, the model parameters are adjusted to best mimic and fit with the training data (model training), and later on, the testing data set is supplied to the trained model with the fine-tuned effective parameters for performance evaluation. The testing and training datasets were utilized for calibration using inlet water temperature, mass flow rates of water, ambient temperature, and the measured temperature outside the insulated storage volume as the variable data input parameters and the outlet water temperature as the output. Once the system models have been developed, the next step is to train them using the training dataset, as shown in Fig. 1. The data set is fed into the system as an input, with arbitrary parameters set within an acceptable range. If the output of the system matches the measured data, the parameters are deemed correct. However, if the output does not agree with the measured data, the system will un-

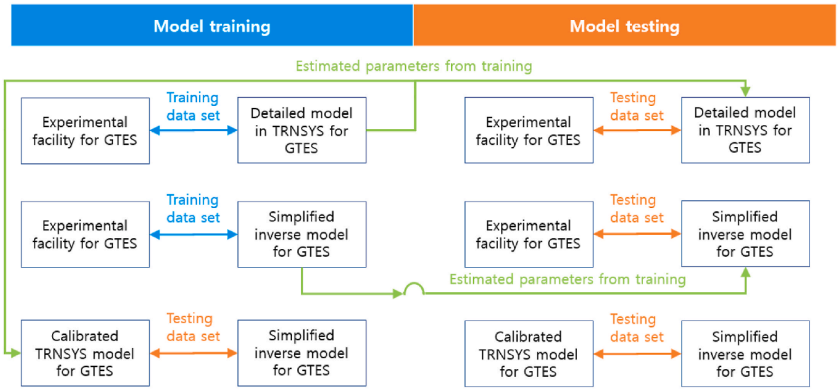

Fig. 1. Model calibration with training processes in this study.

dergo training and testing activities. During the training phase, the algorithm will test various parameters iteratively until the output of the system closely or perfectly matches the output of the measured data. At the completion of each training, the fine-tuned parameters are fed into the system using the training data set, and the unseen testing data sets are employed to test the models for evaluation and validation. For testing the trained model in this study, it is assumed that ambient temperature is perfectly known. To further understand the functioning strategy of the system, it is noteworthy that the objective of the study is to evaluate the performance of the simplified IGB model. Therefore, an experimental facility and a detailed TRNSYS model for shallow UTES with vertical and horizontal configurations were employed as subjects to assess the training performance of the simplified IGB model. The detailed TRNSYS model is trained using measured data from the experimental facility to be utilized as another subject for evaluating the IGB model. The training performance of the IGB model is finally assessed using data measured in the experimental facility. Furthermore, the reason for additionally utilizing the trained TRNSYS model is to evaluate the training performance of the simplified inverse model under more diverse conditions.

2.2. Experimental setup

Vertical U-tube and horizontal UTES installed at the Korean Institute of energy Research was used for this study. Fig. 2 shows the overview of the installation while Fig. 3 describes the experiment and data collection set-up and Fig. 4 shows the system dimensions. The borehole pipes for both configurations were buried 2 m below the earth's surface; however, its total depth is 2.5 m. The vertical configuration consists of 16 U-tube boreholes, with each 4 of them arranged in series, as shown in Fig. 3. Ground dimension of the UTES is 4.0 m x 3.4 m x 2.5 m. Rigid polyurethane foam of thickness, 0.2 m was provided 0.3 m below the earth surface and on the sides of the UTES as insulation to prevent heat losses. For measurement of ground temperature, six resistance temperature detectors (RTDs) sensors of uncertainty ± 0.5 °C were buried vertically downward at a spacing of 0.3 m below the top insulation on the east (TV_E_i), west (TV_W_i), north (TV_N_i), south (TV_S_i), and center (TV_C_i) for the vertical UTES and on the east (TH_E_i), west (TH_W_i), north (TH_N_i), south (TH_S_i), and center (TH_C_i) for the horizontal UTES, where i is the sensor number. To determine the effects of the insulation on the sides of the storage volumes (T_G), temperature sensors are installed 0.2 m thick immediately after the vertical insulation (TV_o_i), horizontal insulation (TH_o_i), and at the center between the two storage volumes. Temperature sensors were installed on the supply and return lines of the fluid to measure inlet and outlet water temperatures. Fig. 4 was drawn to show the setup lines for both heat storage (charging) and heat release (discharging). During *heat storage*, water in the storage tank is heated with an auxiliary heater to a certain temperature and supplied to the UTES through the flow valves, *FhvS*2 and *FhoS*1, for vertical and horizontal UTES, respectively. Temperature sensors, *TveS*2 and *TveR*2 were used for monitoring and measuring the supply and return temperature to and from the ground for the vertical UTES, while sensors *ThoS*1 and *ThoR*1 were installed on the supply and return fluid line of the horizontal UTES for the same purpose. During this time, the flow into the systems is only allowed from the tank through the valves *FvoS*2 and *FhoS*1 for the vertical and horizontal configuration, respectively, and the water supply to the system from the radiator is totally shut off through the flow valves *FhraR*2 and *FhraS*1 for vertical and horizontal configurations,

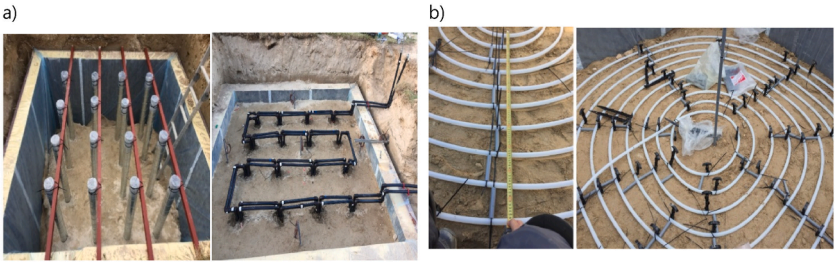

Fig. 2. Installation layout of the field UTES a) Vertical UTES and b) Horizontal UTES.

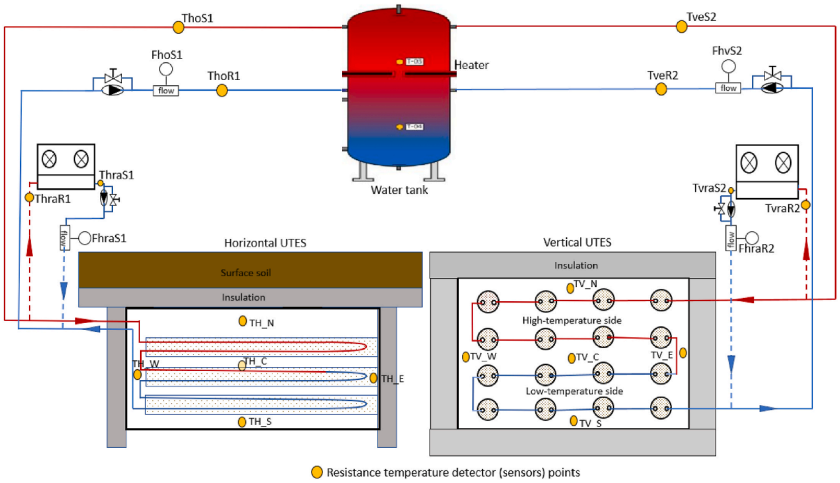

Fig. 3. Experimental set-up.

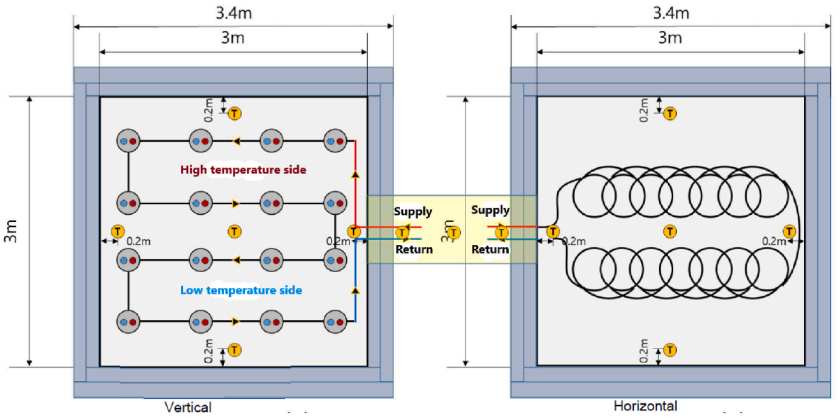

Fig. 4. Representation UTES dimensions.

respectively. Similarly, during the *heat release*, water is supplied to the systems from the radiator through the flow valves, *FhraR*2 and *FhraS*1, for vertical and horizontal configuration, respectively, while the supply and return temperatures were measured using the temperature sensors *TvraS*2 and *TvraR*2 respectively, for vertical and *ThraS*1 and *ThraR*1 respectively for horizontal. During this time, the flow from the tank is shut off completely while supplying the working fluid only from the radiator through the valves *FhraR*2 and *FhraS*1 for vertical and horizontal configurations, respectively. Overall, the flow rates are controlled by valves *FhvS*2 and *FhoS*1 during heat storage, and *FhraR*2 and *FhraR*1 during heat release. The flow into the UTES was regulated between 0 and 550 kg/h, and the flow speed of the fluid was measured using the Magnetic flow meters (magmeters) of uncertainties ± 0.5 kg/h, which are suitable for application on a wide range of liquid types. Detailed analysis of the experimental results will be discussed critically in another study.

2.3. Detailed TRNSYS modeling

A Similar model that represents the experimental setup was developed in the TRNSYS simulation tool for further analysis as shown in Fig. 5. The meteorological data used are the previously measured data specifically for the site. In the detailed model for the vertical UTES configuration, a sixteen-borehole U-tube UTES with the same dimensions was modeled. The horizontal configuration has the same dimension as that of the vertical; however, the total pipe length of 189 m arranged in a slinky pattern was used to correctly align with the actual system. The results were then calibrated using GenOpt [35]. Since the driving parameters of the model such as the thermal conductivity, heat capacity, and density of soil are not known and are difficult and resource-consuming to determine, they were estimated using an optimization method by specifying reasonable lower and upper bounds based on the experimentally determined values in literature [36–40]. For the TRNSYS model, total of four searches were performed using the Hooke-Jeeves Optimization algorithm: mesh size divider = 2; Initial mesh size exponent = 0; mesh size exponent increment = 1; and number of step reduction = 4. Multi-start process was chosen with the random number of seeds chosen as 5 and number of starting points of 4. This implies that four global searches with four optimal values for each of the design parameter of interest will be obtained. The total number of 88 main iterations over the total number of 400 simulations for the same timestep of 1 min were carried out to obtain the results summarized in the result section. In each complete iteration, the optimal values of the design parameters were obtained and docu-

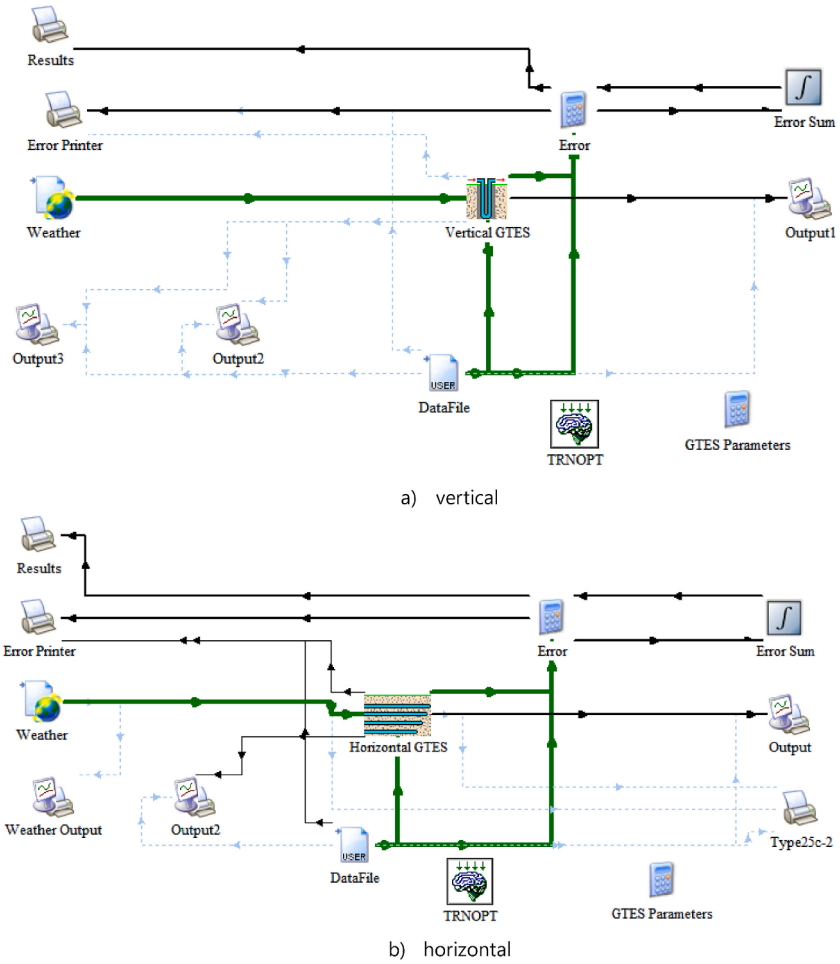

Fig. 5. Detailed TRNSYS Model for a) vertical and b) horizontal configuration.

mented and the best iterate for better calibration were obtained for calculation of the Root Mean Square Error (RMSE) using equation (1) in section 2.5. In addition, the Coefficient of Variation of the RMSE [CVRMSE] were calculated.

2.4. Development of simplified inverse model for vertical UTES

The simplified inverse model for shallow vertical UTES was developed based on the thermal network as shown in Fig. 6. The vertical flow of heat from the ambient air and the horizontal heat flow from/to the far-field were considered for estimation of their thermal resistances. In a U-tube ground heat exchanger, thermal energy from the heat transfer fluid enters through one inlet and exits through the other. The temperature difference between the inlet and outlet temperatures of the working fluid determines the amount of heat, Q_w that is either released or absorbed by the ground, as shown in Fig. 6a. To calculate the mean temperature in the flow channel, the average of the inlet and outlet temperatures is often taken. This mean temperature can then be used to determine the heat interactions between the fluid and the ground. This study simplifies the system by only considering the thermal interactions between the fluid exiting the flow channel and the ground. The simplified system considered five nodes and incorporated four resistances and two capacitances to develop a 4R2C model that can predict the outlet temperature of the system. The 4R2C model was selected to facilitate the analysis of heat transfer in the system, accounting for the transfer within the fluid, pipe, grout, soil, and insulation material. Additionally, heat transfer from the ambient, T_a and far-field outside the insulation T_G were also considered. However, certain assumptions were made during the analysis. Since the ground is considered as a finite or semi-infinite body, the initial ground temperature is considered constant, in order words, constant temperature boundary conditions were considered.

- The effects of ground water were not considered since the system dept is shallow
- Component materials are assumed to be isotropic, homogenous, and categorized by effective parameters
- Fluid-to-pipe and air-to-ground heat transfer is regarded as convection heat transfer only while the heat transfers within the pipe materials, grout, and the ground is by conduction only.

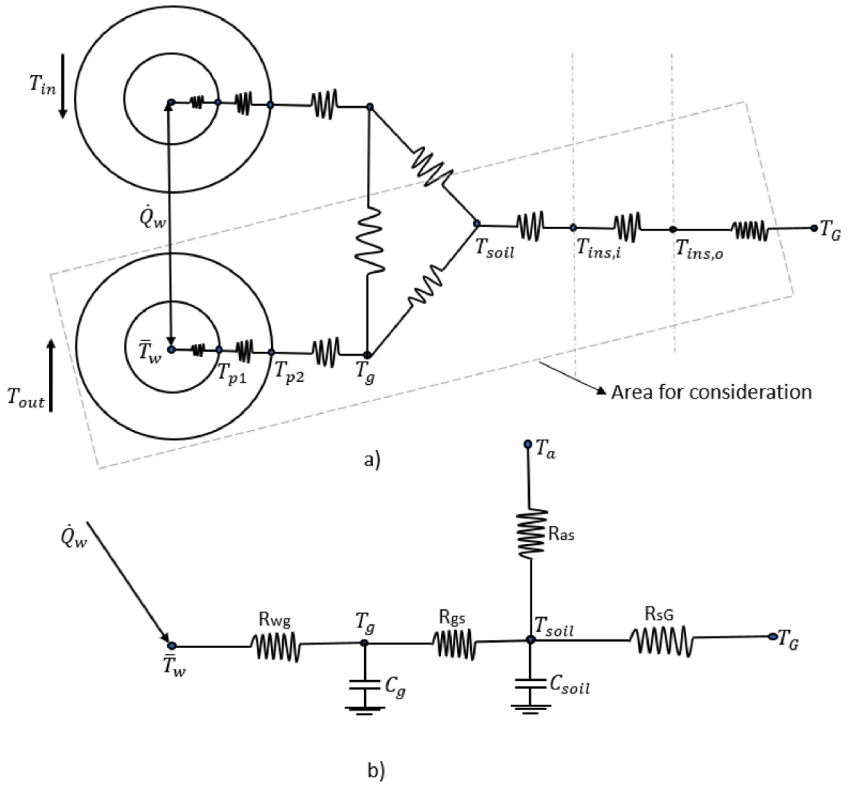

Fig. 6. Simplified 4R2C model for shallow UTES with vertical configuration, a) heat interaction in an underground U-tube heat exchanger and b) thermal network of interest.

$$\text{For Node } \overline{T}_w 0 = \dot{Q}_w + \frac{T_g - \overline{T}_w}{R_{wg}} \tag{1}$$

$$\textit{Where } \overline{T}_w = \frac{T_{in} + T_{out}}{2} \text{ and } \dot{Q}_w = \dot{m}_w c_{pw} \left(T_{in} - T_{out}\right) \tag{2}$$

$$\text{For node } T_g : C_g \frac{dT_g}{dt} = \frac{\overline{T}_w - T_g}{R_{wg}} + \frac{T_{soil} - T_g}{R_{gs}} \tag{3}$$

$$\text{For node } T_{soil} : C_{soil} \frac{dT_{soil}}{dt} = \frac{T_g - T_{soil}}{R_{gs}} + \frac{T_a - T_{soil}}{R_{as}} + \frac{T_G - T_{soil}}{R_{sG}} \tag{4}$$

The effective thermal capacitance of the soil and the grout is given in equations (5) and (6) respectively, where α is a dimensionless factor defined by the user to account for the modification of the thermal inertia [22], Δx is the borehole depth, and V_s is the storage volume defined in [41]

$$\textit{Where } C_{soil} = \rho_s c_{ps} V_s \textit{ with } V_s = N\pi\Delta x\left(0.525 * \textit{borehole spacing}\widehat{)}2\right. \tag{5}$$

$$\textit{Where } C_g = \alpha\rho_g c_{pg} V_g = \alpha\rho_s c_{pg}\pi\left(l_b^2 - 2r_{p_o}^2\right)\Delta x \tag{6}$$

Substituting for T_w and $\dot{Q}_w$ in equation (1) and solving for T_g, equation (7) is obtained. Substituting for T_g in (3) – (4), equations (8) and (9) are obtained for description of the water outlet temperature and the ground temperature.

$$T_g = \left(0.5 - \mathrm{R_{wg}\dot{m}_w c_{pw}}\right) T_{in} + \left(0.5 + \mathrm{R_{wg}\dot{m}_w c_{pw}}\right) T_{out} \tag{7}$$

$$C_g\frac{dT_{out}}{dt}=\left(\frac{1}{R_{wg}+2R_{wg}^2\dot{m}_wc_{pw}}-\frac{0.5-R_{wg}\dot{m}_wc_{pw}}{0.5R_{wg}+R_{wg}^2\dot{m}_wc_{pw}}-\frac{0.5-R_{wg}\dot{m}_wc_{pw}}{0.5R_{gs}+R_{gs}R_{wg}\dot{m}_wc_{pw}}\right)T_{in}+\left(\frac{1}{R_{wg}+2R_{wg}^2\dot{m}_wc_{pw}}-\frac{1}{R_{wg}}-\frac{1}{R_{gs}}\right)T_{out}+\left(\frac{1}{0.5R_{gs}+R_{gs}R_{wg}\dot{m}_wc_{pw}}\right)T_{soil}-C_{grout}\left(\frac{0.5-R_{wg}\dot{m}_wc_{pw}}{0.5+R_{wg}\dot{m}_wc_{pw}}\right)\frac{dT_{in}}{dt}\pm z \tag{8}$$

$$C_{soil}\frac{dT_{soil}}{dt}=\left(\frac{0.5-R_{wg}\dot{m}_wc_{pw}}{R_{gs}}\right)T_{in}+\left(\frac{0.5+R_{wg}\dot{m}_wc_{pw}}{R_{gs}}\right)T_{out}-\left(\frac{R_{as}R_{sG}+R_{gs}R_{sG}+R_{gs}R_{as}}{R_{gs}R_{as}R_{sG}}\right)T_{soil}+\left(\frac{1}{R_{as}}\right)T_a+\left(\frac{1}{R_{sG}}\right)T_G\pm y \tag{9}$$

Where z and y are terms added to account for some unmodeled dynamics and R_{wg} is the resistance from the fluid to the center of the grouting material which is the sum of the thermal resistances of the fluid, pipe and pipe to grout and is expressed mathematically as shown in equations (10) and (11). Further details on the derivation of equations (8) and (9) are provided in the Appendix section.

$$R_{wg}=\frac{1}{A_fh_f}+\frac{\ln\left(r_{p2}/r_{p1}\right)}{2\pi Lk_p}+\frac{\ln\left(r_g/r_{p2}\right)}{2\pi Lk_{grout}} \tag{10}$$

$$\text{and } R_{gs}=\frac{\ln\left(l_b/r_g\right)}{2\pi Lk_{grout}} \tag{11}$$

Where l_b and r_g are the effective distance of the conduction heat transfer path and radius of the grouting material respectively. These are defined mathematically as follows [23]:

$$l_b=\sqrt{r_b^2+\left(\frac{d}{2}+r_p^2\right)^2} \tag{12}$$

$$r_g=\sqrt{\frac{l_b^2+r_p^2}{2}} \tag{13}$$

Similarly, R_{as} and R_{sG} can be expressed based on the resistances on their pathways as follows:

$$R_{as}=\frac{1}{A_sh_{\_air}}+\frac{L_{surf,ins}}{A_{surf,ins}k_s}+\frac{L_{ins}}{A_{ins,top}k_{ins}}+\frac{L_{ins,s}}{A_{ins,s}k_s} \tag{14}$$

$$R_{sG}=\frac{L_{s,ins}}{A_{s,ins}k_s}+\frac{L_{ins}}{A_{ins,side}k_{ins}}+\frac{L_{ins,G}}{A_{ins,G}k_s} \tag{15}$$

Considering T_g to be the temperature of the soil near the pipe and T_{soil}, the temperature of the soil farther away from the pipe, with some more modifications as shown in Fig. 7, the model can be tested for the horizontal configuration using the experimental configurations and dimensions.

The derived model was modeled in MATLAB Simulink while assuming that the change in the inlet temperature with time ($\frac{dT_{in}}{dt}$) is negligible since water at a constant temperature was supplied to the UTES during the field experiment. Parameters of the model ($k_g,\ k_{ins}, k_p, k_s, \rho_g, \rho_s, c_{pg}, c_{ps}, h_{air}, h_f, y, and\ z$), were estimated through training by using the measured input data (T_{in}, $\dot{m}_w$, T_a, *and* T_G) to predict the output (T_{out}) as demonstrated in Fig. 8. The ground temperature, T_G in this model can be modeled as an average constant effective ground temperature of the far-field, outside the insulation, representing the typical underground temperature. Therefore, in the case where T_G is unknown, for example, using the TRNSYS-generated data for training and testing the inverse model, the average value of measured T_G over a long period is used as a constant value with an assumption that the insulation is capable of keeping the temperature within the range. Nonlinear optimization method which uses the Trust-Region-Reflective algorithm (TRRA) was used for the investigation. TRRA is the best algorithm to use when the provision of the gradient is required as it allows only upper and lower bounds or linear equality constraints; hence, it is the best algorithm for the model evaluation. The objective function used to calibrate the models was the sum of squared error (SSE) shown in equation (18). The RMSE and CVRMSE were calculated to evaluate calibration.

2.5. Performance index

The performance of the energy system model is driven by statistical models such as the coefficient of determination (R^2), root mean square error (RMSE), coefficient of variation of the mean square error (CVRMSE), and mean bias error (MBE) [42]. R^2 is useful for system prediction using regression analysis, whereas, in comparison to the rest, RMSE, which uses the sum of square error (SSE) between the baseline and the predicted values for a measure of accuracy, appears to be commonly used [42–45]. The CVRMSE is the

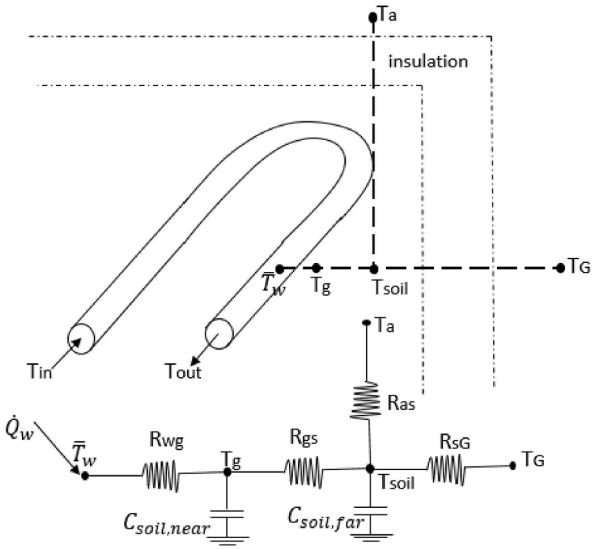

Fig. 7. Simplified 4R2C model for shallow UTES with horizontal configuration.

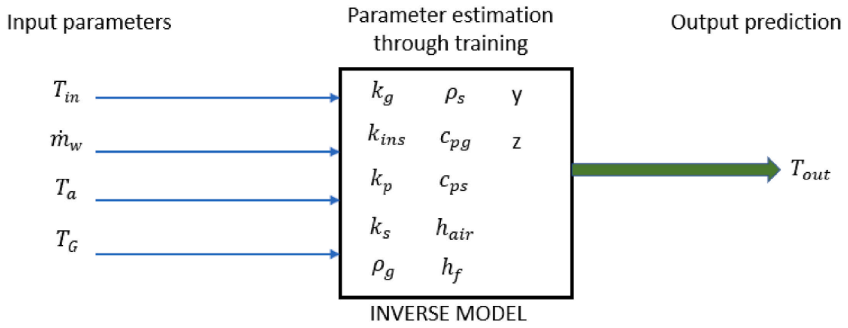

Fig. 8. Relationship between the input parameters, driving parameters to estimate, and output parameter for calibration of the proposed model.

normalized form of the RMSE using the mean or the range of the actual values to account for the dependency of the RMSE on the data scaling. Although results less than 20 % is acceptable, the lower, the better [40]. In general, the time-variant objective function, J(t), for the SSE is defined over the temperature changes as shown in equation (19). Mathematically, the objective function J(t) for model calibration, which is equivalent to SSE, RMSE, and CVRMSE for the study, are given in equations (19)–(21), respectively.

$$J = SSE = \sum_{i=1}^{N} (error\ (i))^2 = \sum_{i=1}^{N} \left(T_{out,sim}(i) - T_{out,exp}(i)\right)^2 \quad i = 1, \ldots, N \tag{20}$$

$$RMSE = \sqrt{\frac{\sum_{i=1}^{N} \left(T_{out,sim} - T_{out,exp}\right)^2}{N}} \tag{21}$$

Where, N = Number of non-missing data points, and i is the current timestep. As the name implies, $T_{out,sim}(i)$ is the predicted outlet temperature from the model simulation for the i^{th} timestep at the time, t and $T_{out,exp}(i)$ represents the measured outlet temperature from the actual system for the time-step, i.

The Coefficient of Variation of the RMSE is given as:

$$CVRMSE = \left(\frac{RMSE}{\overline{T}_{out,exp}}\right) * 100 \tag{22}$$

$\overline{T}_{out,exp} = Average\ measured\ temperature\ over\ the\ time - step$

3. Results and discussion

3.1. Detailed TRNSYS model calibration with experimental data

Detailed TRNSYS model for both system configuration was developed and calibrated using the data obtained from experiment carried out between December 15 to December 31, 2021 to ensure consistency in the data and optimization accuracy. However, the model was tested using the experimental data obtained between March and April 2023 consisting of first heat storage, first heat release and second heat storage. The result of the calibrated model is as shown in Fig. 9 for training and testing operations while the initial guess and optimized parameters are shown in Table 1. The detailed TRNSYS model showed good agreement on both configurations however, for the horizontal configuration, there was a rapid increase in the outlet water temperature during heat storage, especially for the testing operation, deviating a little from the experimental data. This behavior can also be noticed during heat release, where the simulated value appears a little above the experimental value with the optimized parameters. Although this deviation exists, the RMSE of the systems during training indicated good calibration with values of 0.87 °C and 0.49 °C for vertical and horizontal configurations respectively and CVRMSE of 1.38 % and 0.80 % respectively. For testing, the RMSE was 0.95 °C corresponding to

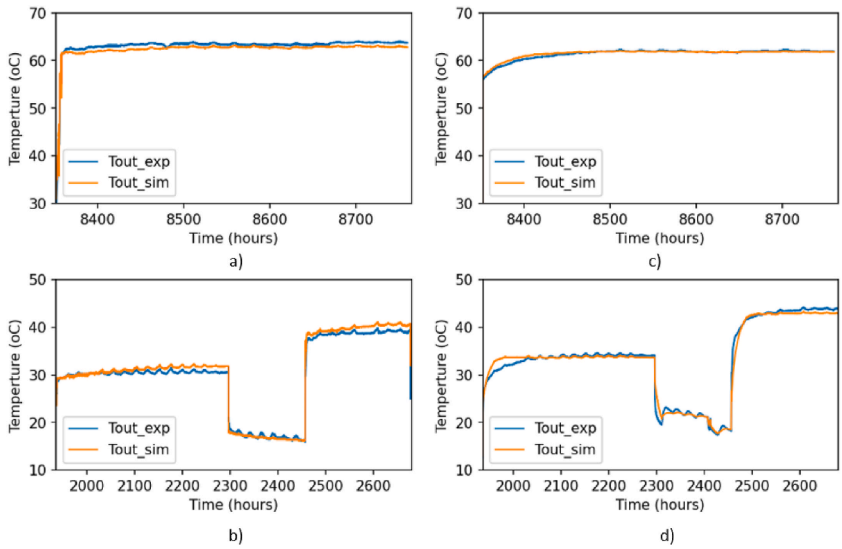

Fig. 9. Training and testing results for detailed TRNSYS model calibration with experimental data for vertical and horizontal configuration, a) vertical training, b) vertical testing, c) horizontal training, and d) horizontal testing.

Table 1
Optimized parameters with initial guesses.

Vertical				
Parameters	Lower bound	Upper bound	Initial guess	Optimized value
Pipe inside diameter (m)	–	–	0.024	0.024
Pipe outside diameter (m)	–	–	0.032	0.032
Total length of pipe (m)	–	–	56.00	56.00
Storage Volume (m^3)	–	–	22.17	22.17
Borehole depth (m)	–	–	2.50	2.50
Thermal Conductivity soil (kJ/hr·m·K)	4.60	20.00	4.80	15.975
Volumetric Heat Capacity of soil (kJ/m^3/K)	2000.00	6000.00	3600.00	5950.01
Thermal conductivity of grout (kJ/hr·m·K)	2.50	12.00	4.00	2.50
Thermal conductivity of insulating material (kJ/hr·m·K)	0.15	0.80	0.20	0.15
Thermal conductivity of pipe (kJ/hr·m·K)	1.44	12.00	3.60	11.147
Horizontal				
Pipe inside diameter (m)	–	–	0.014	0.014
Pipe outside diameter (m)	–	–	0.018	0.018
Total length of pipe (m)	–	–	189.00	189.00
Borehole depth (m)	–	–	2.50	2.50
Thermal conductivity of pipe (kJ/hr·m·K)	0.8000	2.40	1.36	0.849
Specific heat of soil layer (kJ/kg·K)	0.4000	32.00	0.84	23.60
Density of soil (kg/m^3)	1200.00	6000.00	2100.00	4616.18
Thermal conductivity of soil (kJ/hr·m·K)	1.4000	7.50	4.68	4.675
R-value of insulating material (h·m^2·K/kJ)	2.3148	2.3148	2.32	2.3148

CVRMSE of 3.16 % for the vertical configuration and 0.99 °C, corresponding to CVRMSE of 2.97 % for the horizontal configuration as shown in Fig. 12.

3.2. Inverse grey-box model training with experimental data

Similarly, the optimal parameter estimation was carried out for the simplified IGB model using recent experimental data, the same as in the previous section for the detailed TRNSYS model versus measured data. For model testing, experimental data obtained between March and April 2023 consisted of first heat storage, first heat release, and second heat storage, as in the previous section was used. Table 2 shows the estimated parameters together with their initial guesses, while Fig. 10 shows the training and testing results as obtained. During training and testing for vertical and horizontal configurations, the IGB model showed good agreement with the

Table 2
Estimated Parameters including the initial guesses.

vertical Configuration				
Parameters	initial value	final value	Initial guess	Estimated value
Thermal conductivity of grout (kJ/hr·m·K)	2.50	12.00	4.60	2.5150
Thermal conductivity of insulating material (kJ/hr·m·K)	0.20	0.80	0.40	0.1501
Thermal conductivity of pipe (kJ/hr·m·K)	1.44	12.00	2.50	11.443
Thermal Conductivity soil (kJ/hr·m·K)	4.60	16.00	4.60	15.60
Density of grout (kg/m^3)	2000.00	10000.00	2500.00	7865.0
Density of soil (kg/m^3)	2000.00	10000.00	2500.00	7368.8
heat capacity grout (kJ/kg·K)	3.50	300.00	8.60	115.34
heat capacity soil (kJ/kg·K)	3.50	300.00	8.60	66.565
heat transfer coefficient of air (kJ/hr· m^2·K)	9.00	90.00	24.00	36.00
heat transfer coefficient of fluid (kJ/hr·m^2·K)	14700.00	32000.00	14000.00	19209.00
y	-inf	inf	0.00	0.0055975
z	-inf	inf	0.00	−0.0003351
Horizontal Configuration				
Thermal conductivity of grout (kJ/hr·m·K)	2.50	12.00	4.60	2.5150
Thermal conductivity of insulating material (kJ/hr·m·K)	0.20	0.80	0.40	0.15
Thermal conductivity of pipe (kJ/hr·m·K)	1.44	12.00	2.50	11.44
Thermal Conductivity soil (kJ/hr·m·K)	4.60	16.00	4.60	15.60
Density of grout (kg/m^3)	2000.00	10000.00	2500.00	7944.6
Density of soil (kg/m^3)	2000.00	10000.00	2500.00	4283.3
heat capacity grout (kJ/kg·K)	3.50	300.00	8.60	102.62
heat capacity soil (kJ/kg·K)	3.50	300.00	8.60	76.449
heat transfer coefficient of air (kJ/hr·m^2·K)	9.00	90.00	24.00	36.00
heat transfer coefficient of fluid (kJ/hr·m^2·K)	14700.00	32000.00	14000.00	19209.00
y	-inf	inf	0.00	0.0083306
z	-inf	inf	0.00	−0.002206

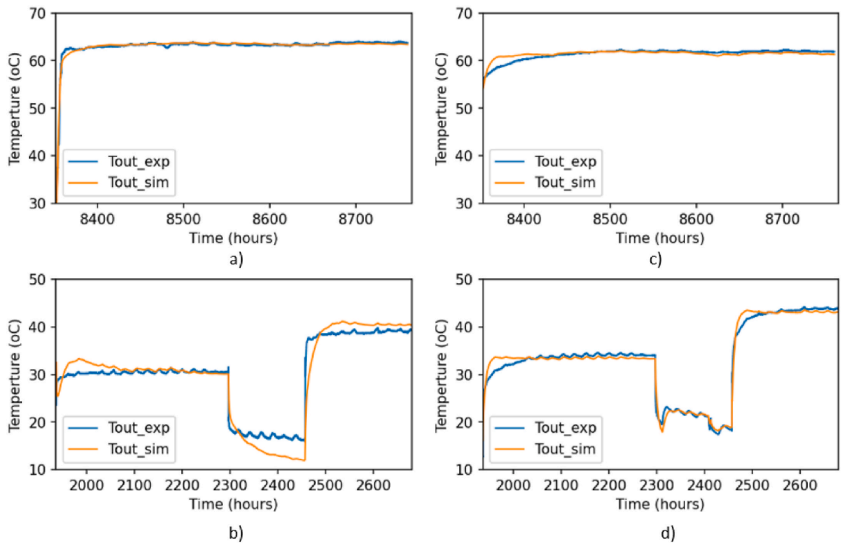

Fig. 10. Training and testing result for IGB model calibration with experimental data for vertical and horizontal configurations, a) vertical training, b) vertical testing, c) horizontal training, and d) horizontal testing.

field experimental data, although with some discrepancies. For the vertical configuration, a little discrepancy was observed during the model training, especially during the initiation of the heat storage or release, leading to an RMSE of 0.46 °C corresponding to a CVRMSE of 0.72 %. Conversely, the horizontal configuration exhibited a lower performance during training by increasing and decreasing gradually with the experimental data during the heat storage and heat release, respectively, while maintaining stability. The predicting performance indicated an RMSE of 0.67 °C corresponding to a CVRMSE of 1.09 % during training, as summarized in Fig. 12. In Fig. 12, it can be observed that there is a significant increase in CVRMSE from 0.72 % for training to 7.91 % during testing for the vertical configuration, similar to the comparison between the measured data and detailed TRNSYS model. Additionally, for the horizontal configuration, the CVRMSE increased from 1.10 % during training to 3.17 % during testing.

3.2.1. Time-wise variation of error

For further visualization of the system behavior, the change of errors over the simulation periods for training and testing operations is shown in Fig. 11, following the objective function defined in this study. In training operations (Fig. 11 a), the error is more encountered at the beginning of the data points but approaches a zero value over time. Similar to the training operation, the error during the testing was encountered at the beginning of the simulation time. However, this overshoots during the transition from heat storage to heat release and vice versa, as can be observed in Fig. 11 b). In general, the error overshoot at the beginning and during the transition phases for training and testing operations are higher for the vertical configuration, indicating a lower performance. This behavior for both configurations can be attributed to the turbulence in the flow during these transitions.

3.3. Inverse grey-box model training with calibrated detailed TRNSYS model

3.3.1. Summary of the model calibration performance

The training output of the TRNSYS model, which was trained using measured data, was utilized to train the IGB model. The testing output of the TRNSYS model was used to test the IGB model after its training, and similar graphical results were obtained. A summary of the training and testing results of all models is provided in Fig. 12.

For the training operation conducted on the vertical configuration, the IGB model trained with the measured data yielded the best results, followed by the detailed TRNSYS model trained with measured data, and finally, the IGB model trained with data generated from the calibrated TRNSYS model. The CVRMSE values obtained for the vertical configuration were 0.72 %, 1.38 %, and 1.40 %, respectively, as shown in Fig. 12 a). In contrast, for the horizontal configuration, the detailed TRNSYS model trained with measured data yielded the best results, followed by the IGB model trained with the detailed TRNSYS model, and finally, the detailed TRNSYS model trained with the measured data. The CVRMSE values obtained were 0.80 %, 0.86 %, and 1.10 %, respectively, as shown in Fig. 12 b). For the testing operation of the vertical system, the detailed TRNSYS model trained with measured data for the vertical configuration performed best. This was followed by the inverse model trained with TRNSYS-generated data, and then the IGB model trained with the measured data. The CVRMSE values for these comparisons were 3.16 %, 5.42 %, and 7.91 %, respectively. For the horizontal type, the TRNSYS model was found to be the most effective method when tested with the measured data. This was followed by the

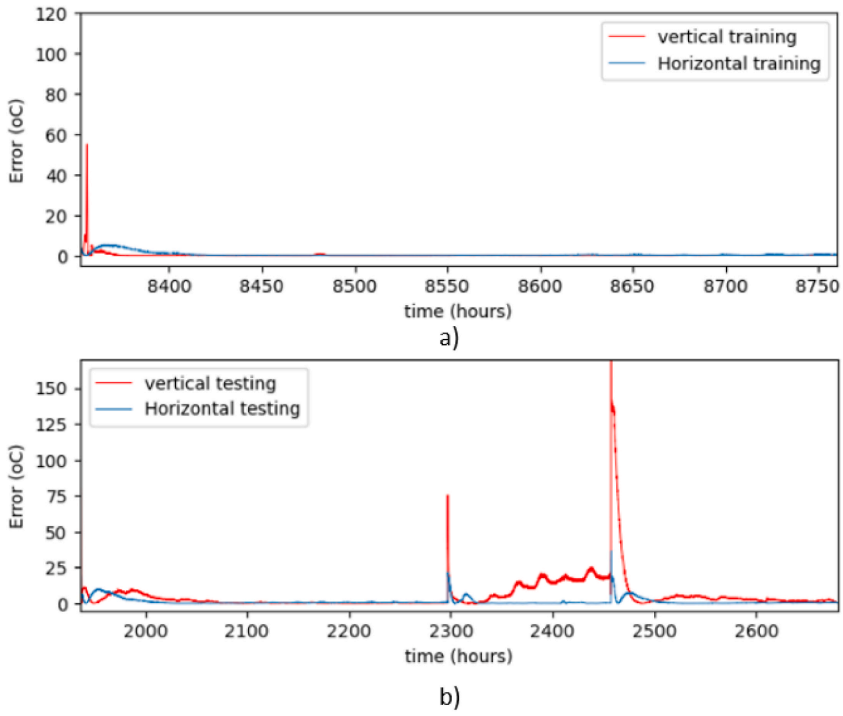

Fig. 11. Time-wise variation of the error used for calculation of the objective function for horizontal and vertical configurations a) Training period b) Testing period.

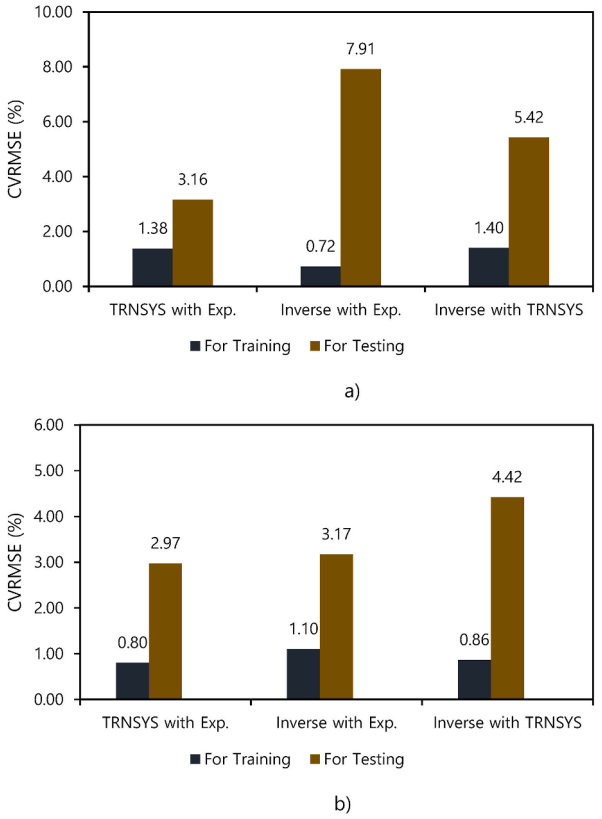

Fig. 12. Comparison of the CVRMSE for training and testing results a) vertical and b) horizontal.

IGB model trained with measured data and then the IGB model trained with the detailed TRNSYS model. The CVRMSE values for these comparisons were 2.97 %, 3.17 %, and 4.42 %, respectively. These variations in error rates may be due to the nature of the data since the testing data was over a longer period than the training data and contains a longer period of heat release. Further investigation was conducted through a comprehensive durability test of both the training and testing operations. The results of the test are provided in the following section.

3.3.2. Effects of training and testing duration on the model performance

The detailed TRNSYS model, which was calibrated with measured data, was used to generate data. This data was then utilized to train and test the IGB model for the vertical configuration to enhance the understanding of the system dynamics. In general, 24 weeks (Jan. 1 – June 18) simulation was carried out for the data generation. For the training duration test, the last 12 weeks (March 26 – June 18) were fixed and were used for evaluating the model after each training. The inlet temperature was fixed at 40 °C, 50 °C, and 60 °C during the first, second, and third heat storage phases, respectively, while the inlet temperature during every heat release was fixed at 15 °C. The first 12 weeks were divided into four training datasets. The first dataset was for four weeks (Feb. 26 – March 25), with a heat storage inlet temperature of 35 °C for two weeks, and a heat release inlet temperature of 15 °C for the remaining two weeks. The second training dataset was extended for six weeks (Feb. 12 – March 25), during which there were two weeks of heat storage at an inlet temperature of 35 °C, two weeks of heat release at an inlet temperature of 15 °C, and two weeks of heat storage at an inlet temperature of 45 °C. Third and fourth training datasets were allocated 8 and 12 weeks, respectively, with detailed information on heat release and heat storage inlet temperatures in Table 3. Flow rates of 420 kg/h and 200 kg/h were respectively applied for the heat storage and release phases. As indicated in Fig. 13 tests 1 through 4 in the training duration test yielded CVRMSE values of 7.0 %, 5.5 %, 4.8 %, and 4.4 %, respectively. In general, during training, the error increases linearly with the training duration, and during testing, it decreases linearly with the training duration, as shown in Fig. 15 a). These results demonstrate that extended training durations improve the model's accuracy in predicting outlet temperatures (see Table 4).

During the performance evaluation for the testing duration test, the first 12 weeks (Jan. 1 – March 25) were fixed after training. The last 12 weeks (March 26 – June 18) were used for testing, during which the testing duration changed. The trained dataset consisted of three heat storage phases, each carried out over two weeks with inlet temperatures of 35 °C, 45 °C, and 55 °C, respectively. Additionally, there were three heat release phases, each simulated over two weeks with an inlet temperature of 15 °C. The first testing duration lasted for 4 weeks (March 26 – April 23), followed by 6 weeks (March 26 – May 7), 8 weeks (March 26 – May 21), and 12 weeks (March 26 – June 18), as described fully in Table 3. Similarly, test 1 through 4 for the testing duration test shows CVRMSE of 3.1 %, 3.0 %, 4.0 %, and 4.0 % (Fig. 14). To compare the training and testing errors, it is important to note that the training error re-

Table 3
Training and testing duration test data description.

Training duration test (test data fixed)	Description
Fixed Testing dataset (March 26 – June 18)	Two weeks heat storage (40 °C) - two weeks heat release (15 °C) - two weeks heat storage (50 °C) - two weeks heat release (15 °C) - two weeks heat storage (60 °C) - two weeks heat release (15 °C)
Training 1 (Feb. 26 – March 25)	Two weeks heat storage (35 °C) - two weeks heat release (15 °C)
Training 2 (Feb. 12 – March 25)	Two weeks heat storage (35 °C) - two weeks heat release (15 °C) - two weeks heat storage (45 °C)
Training 3 (Jan. 29 - March 25)	Two weeks heat storage (35 °C) - two weeks heat release (15 °C) - two weeks heat storage (45 °C) - two weeks heat release (15 °C)
Training 4 (Jan. 1 - March 25)	Two weeks heat storage (35 °C) - two weeks heat release (15 °C) - two weeks heat storage (45 °C) - two weeks heat release (15 °C) - two weeks heat storage (55 °C) - two weeks heat release (15 °C)
Testing duration test (train data fixed)	Description
Fixed Trained dataset (Jan. 1 – March 25)	Two weeks heat storage (35 °C) - two weeks heat release (15 °C) - two weeks heat storage (45 °C) - two weeks heat release (15 °C) - two weeks heat storage (55 °C) - two weeks heat release (15 °C)
Testing 1 (March 26 – April 23)	Two weeks heat storage (40 °C) - two weeks heat release (15 °C)
Testing 2 (March 26 – May 7)	Two weeks heat storage (40 °C) - two weeks heat release (15 °C) - two weeks heat storage (50 °C)
Testing 3 (March 26 – May 21)	Two weeks heat storage (40 °C) - two weeks heat release (15 °C) - two weeks heat storage (50 °C) - two weeks heat release (15 °C)
Testing 4 (March 26 – June 18)	Two weeks heat storage (40 °C) - two weeks heat release (15 °C) - two weeks heat storage (50 °C) - two weeks heat release (15 °C) - two weeks heat storage (60 °C) - two weeks heat release (15 °C)

Table 4
Summary of selected previous model and results.

Authors	Model Type	Method of evaluation	RMSE (^{o}C)	CVRMSE (%)
Kim et al. [25]	Numerical Model	Calibration against FEFFLOW model	0.13	1.33
Maestre et al. [22]	R–C model	Calibrated against ANSYS model	0.41	Not calculated
Maestre et al. [23]	R_C model	Calibrated against ANSYS model	0.41	Not calculated
Naranjo-Mendoza et al. [46],	Analytical and Numerical models	Compared with experimental data	Range: 0.1–11.56	NRMSE: Range 1.82–163.68
Baser and McCarthy [47]	Numerical Modeling	Calibration and validation with experimental data	Graphical comparison	Graphical comparison
Lamarche [48]	Modified finite line source	Analytical vs COMSOL model	Graphical comparison	Graphical comparison
Najib et al. [49]	Capacitance Resistance Model (CaRM) vs CFD	Calibrated with ANSYS CFD model	0.29	Not calculated
Miao et al. [50]	Grey-box and white box model	Calibrated with field data	Grey-box = 0.96 White-box = 0.78	Not calculated

mains constant as its duration is fixed. On the other hand, the testing error fluctuates irregularly within an acceptable range as the duration of testing changes. Fig. 15 b) shows that the highest error was observed in test 3, followed by tests 4, 2, and then 1. This result suggests that if we train the dataset for an extended period and evaluate the model's performance using datasets within the training duration, the error remains within an acceptable range with minimal deviations. Therefore, the duration of the testing data has an impact on the model's ability to predict the outlet temperature accurately.

3.3.3. Long-term performance comparison of detailed TRNSYS model and IGB model

The performance of the detailed TRNSYS model was assessed against an IGB model over a 10-year period, using an hourly timestep under the same conditions as shown in Fig. 16. For this long-term performance test, a trained duration of 12 weeks (Jan. 1 – March 25) as described for the fixed trained dataset in Table 3 was used. Throughout this duration, the models simulated three heat storage periods with inlet temperatures of 40 °C, 50 °C, and 60 °C, each corresponding to three heat release periods with a consistent inlet temperature of 15 °C, as outlined in Table 3, row 2. Each storage and release cycle lasted two weeks, with flow rates set at 420 kg/h for storage and 200 kg/h for release. This entire cycle repeated until the end of the 10-year period. The simulation results are depicted in Fig. 16 a) with a zoomed graph to five years for clearer observation in Fig. 16 b). The comparison revealed good agreement between the charging and discharging periods, although deviations increased slightly with each subsequent storage and release cycle. The assessment of both models over this period yielded a Coefficient of Variation of Root Mean Square Error (CVRMSE) of 5.2 %, indicating satisfactory performance over the extended duration of the study.

Additionally, to identify the optimal training duration that yields satisfactory performance over a long-term (10 years) testing period, model training at different durations ranging from 4 to 24 weeks was conducted, as depicted in Fig. 17. The findings revealed a clear trend: shorter training durations correlated with higher CVRMSE values in long-term performance assessment. However, as the training duration is extended, convergence of errors is observed, indicating an improvement in performance stability. Although the use of a short range of training data to make a long-term prediction yielded a performance that is within acceptable accuracy, the observed trend of higher CVRMSE values with shorter training durations underscores the importance of allowing sufficient time for the

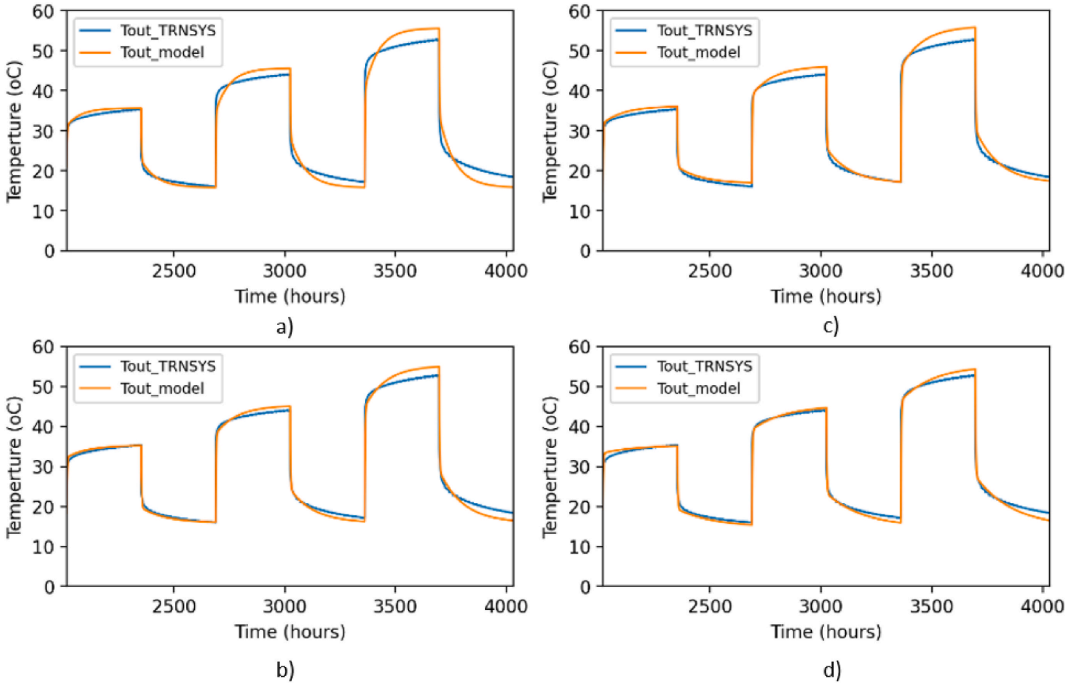

Fig. 13. Effects of training duration on the model performance a) Training 1 (CVRMSE = 7.0 %) b) Training 2 (CVRMSE = 5.5 %) c) Training 3 (CVRMSE = 4.8 %), and d) Training 4 (CVRMSE = 4.0 %).

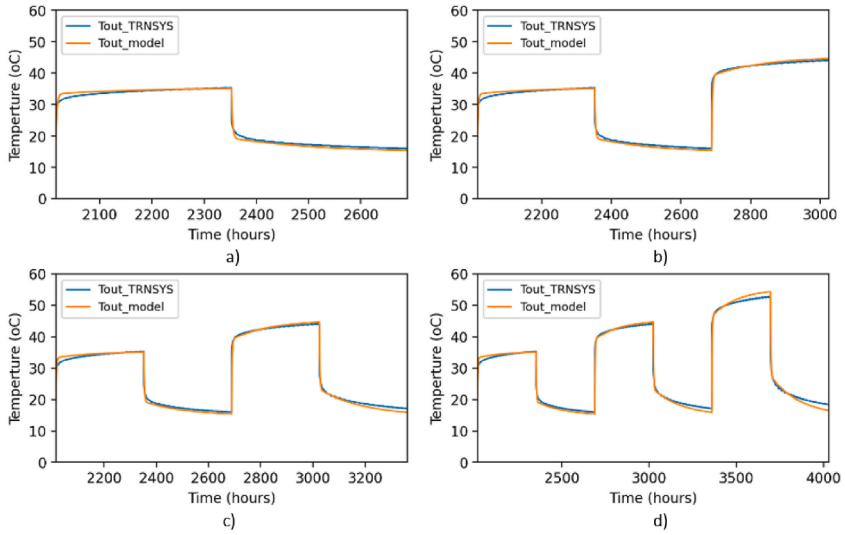

Fig. 14. Effects of testing duration on the model performance a), Testing 1 (CVRMSE = 3.1 %), b) Testing 2 (CVRMSE = 3.0 %), c) Testing 3 (CVRMSE = 4.0 %), and d) Testing 4 (CVRMSE = 4.0 %).

model to learn and adapt to the underlying patterns in the data. When the training duration is limited, the model may not have the opportunity to fully capture the complexities of the data, leading to higher errors in long-term predictions. Conversely, the convergence of errors as the training duration increases suggests that longer training periods enable the model to refine its parameters and better generalize to unseen data. In this study it indicates that beyond 20 weeks, further training yields little or no improvement in performance, as the model converges in its learning curve. Even at that, the results obtained using the short range of data for training in this study remained at an acceptable accuracy. However, the result is crucial for balancing computational resources and performance requirements. Investing too little time in training may result in suboptimal performance, while excessively long training durations may incur unnecessary computational costs without significant improvements in performance. Moreover, this point of convergence of 20 weeks can be considered a short period of training that predicts the model's output over a long period, which is an edge that the inverse grey-box model holds over other machine learning models, such as the ANN. Although the long-term predictive performance

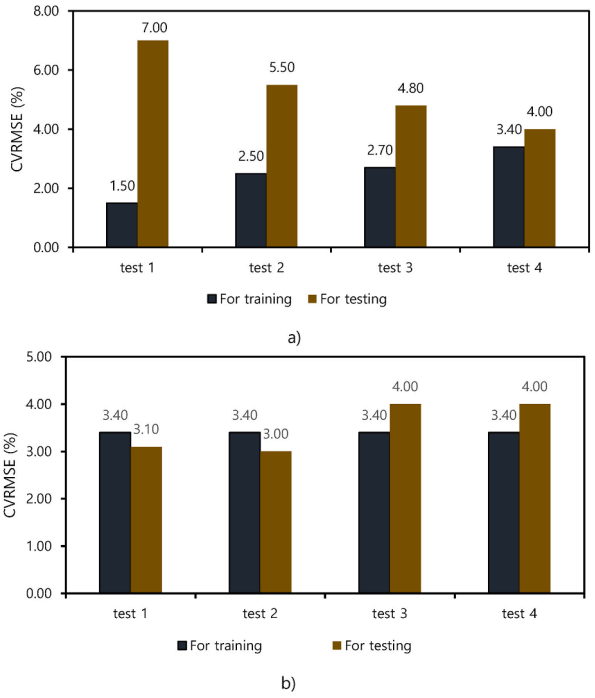

Fig. 15. Training and Testing CVRMSE Comparison: a) Training duration test and b) Testing duration test.

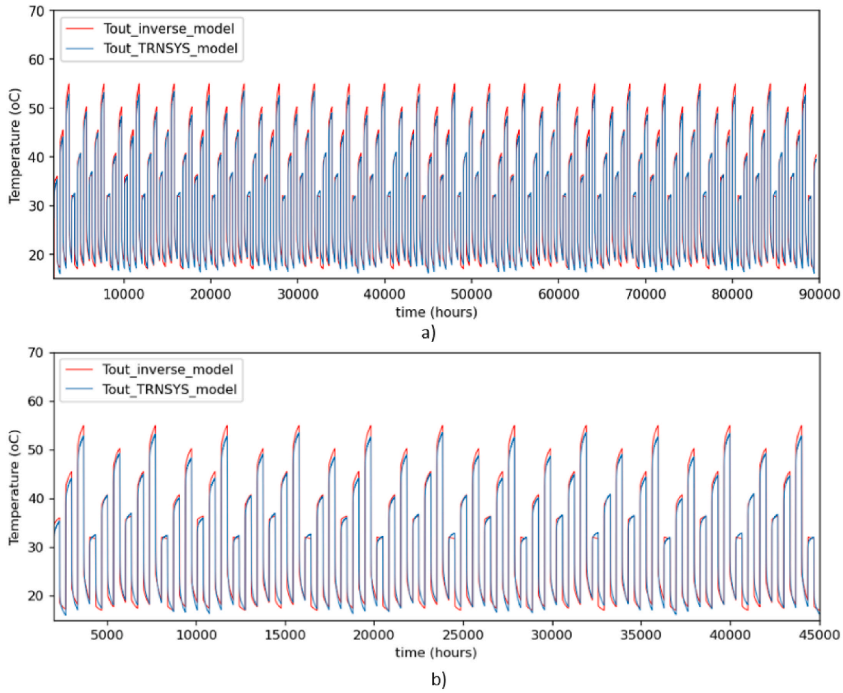

Fig. 16. Ten years Performance evaluation of the detailed TRNSYS model and inverse model, a) Ten years test result (CVRMSE = 5.2 %) and b) Zoomed figure of first five years result.

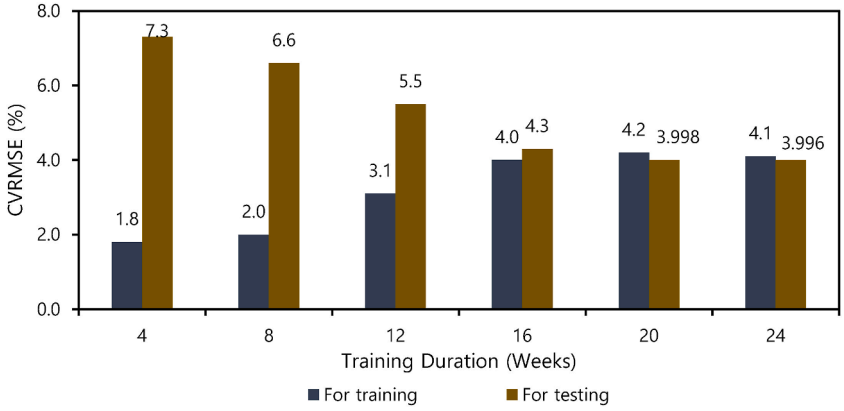

Fig. 17. Impact of training duration on long-term performance.

obtained in this study is within the acceptable accuracy, updating the model's learning outcomes with recent data at appropriate intervals may also be applicable, which could address cases where long-term prediction performance accuracy is low.

3.4. Justification of the deviations between measured and simulated data

Although the calibrated models provided errors that are within the accepted limits, the existing deviations between the simulated and measured results require scientific justification. Often, the deviations between model predictions and measured data in system modeling are due to various factors that highlight the complexities of accurately simulating real-world systems. In this study, the obtained results are believed to have been influenced by the factors which include model structure uncertainty, where the model may have oversimplified the system's behavior due to necessary assumptions such as the approximated value of T_G used when it is unknown, leading to gaps between predictions and actual observations. The uncertainties in the specified parameters and the experimental data used for calibrating and validating the models also played a significant role. The experimental data may contain errors or noise due to the uncertainties in the measuring equipment, contributing to discrepancies. Furthermore, inaccuracies in specifying initial and boundary conditions as well as the numerical approximations and computational limitations required for solving complex models such as the detailed TRNSYS model, may have introduced additional errors thereby affecting the model outcomes. Finally, external factors such as the dynamics that are not considered during the modeling process or changes in the system over time may also have led to certain deviations.

3.5. Comparison with other studies

Previous studies have presented various models for analyzing the performance of different geometric configurations of UTES systems, and these models have been successfully validated. Finite difference, finite volume and finite element method [51], with the aid of various computer software such as ANSYS [22,23,52], FEFLOW [25,53], etc. have been used to study the heat transfer profile of systems. However, some of these models may be complex and challenging for engineers to understand and apply. Therefore, there is a need for a simplified model that can provide accurate predictions within an acceptable range of deviations. It is important to emphasize that there's no universal benchmark to determine the optimal RMSE across all scenarios. The assessment of what constitutes a good RMSE relies heavily on factors such as the characteristics of the validation data and the intricacies of the specific problem at hand. Nevertheless, ASHRAE standards offer a standardized acceptable range for validating energy systems [40]. The objective of this review is to further validate the calibration results obtained in the current study. In this regard, several models from previous works, as shown in Table 4, were reviewed and compared with the findings of the present study. For instance, the work of Kim et al. [25], predicted the outlet water temperatures with RMSE and CVRME of 0.13 and 1.33 %, respectively. In another previous work by Maestre et al. [22,23], R–C models for predicting exit water temperature of a UTES, as well as the ground temperature was developed The authors considered the double-sided heat transfer from both inlet and exit U-tube pipes to the borehole radius, with nodes located at the center of the pipes, the grout material, and the borehole radius. The predictive model was compared with similar models developed in ANSYS CFD tool and the result predicted outlet water temperature with RMSE of 0.41 and 0.19 respectively although the CVRMSE was not calculated. The work of Najib et al. [49] developed a Capacitance Resistance model (CaRM) for a large helical UTES for predicting the core and bore wall temperatures. The system was corroborated against a similar model developed in ANSYS while both models were simulated using the field experimental data of same geometry. The study produced a model with RMSE of 0.29 °C as indicated in Table 4. Miao et al. [50] developed a second order state space model for application with the ground source heat exchanger solving for the hot and cold outlet temperatures by the use of both white- and grey-box models. The white- and grey-box model predicted outlet temperatures of the hot side with error of 0.78 and 0.96 respectively. Naranjo-Mendoza et al. [46] compared various numerical models, such as sinusoidal, semi-infinite, and finite difference methods (FDM), to forecast ground temperature changes over both short and long periods. They measured data hourly at depths ranging from 0.75 m to 2.75 m. The RMSE and NRMSE for all models ranged between 0.1 and 11.56 °C and 1.82–163.68 % respectively. However, the FDM model was found to be the least accurate. In a study conducted by Baser and McCarthy [47], a dynamic soil temperature was simulated within field-scaled SBTES that contained 15 m deep ground heat exchangers spaced 1.5 m apart. The numerical models used in the study were calibrated

based on the field experiment, and the results showed that the simulated soil temperature closely matched the measured data. Lamarche [48] modified the finite line source method for a horizontal UTES and calibrated it against a detailed COSMOL model. The graphical results of the analytical model showed good agreement to those of the detailed COMSOL model [54].

As previously mentioned, previous studies have achieved success in modeling UTES systems; however, none of them focused on shallow UTES. Additionally, some of these models are complex and may pose challenges in terms of comprehension and application. Moreover, their validation periods have been relatively short compared to the current study, which conducted model testing over a period of 10 years. One significant challenge in UTES applications is the considerable thermal energy loss, particularly from the top and sides of the storage volume. It is also crucial to perform sensitivity analysis to ascertain the model dynamics of certain variables. While previous models agreed with validation data, insulation, and parameter sensitivities were under-explored. In contrast, the present work derived a model that considers both the top and side insulation of the storage volume. This approach was based on the training and testing data obtained from the field experiment, which were also used to validate the model. Furthermore, the study investigated how the model's performance is affected by the duration of training and testing over short and long-term performance which is a limitation to other machine learning models such as the ANN.

4. Conclusion

In this study, experimental investigation of improved shallow vertical and horizontal configurations of UTES was conducted for model calibrations. Detailed TRNSYS models and simplified thermal network-based 4R2C IGB models representing the field experiment were developed and calibrated using the data from the field experiment. The calibrated results were analyzed and compared with other few models in literature. The summary of the study based on the analysis carried out is given as follows:

- The installation of 0.2 m thick polyurethane foam insulation improved the performance of UTES systems, validating the use of their measured data for model calibration.
- In comparing the calibrated models, the IGB model trained with the measured data for the horizontal configuration performed best, followed by the detailed TRNSYS model trained with the measured data. For the vertical configuration, the detailed TRNSYS model trained with the measured data performed best, followed by the IGB model trained with the measured data. Although the calibration performance differs for each case, the calibrated models agreed with the field experimental data to an applicable degree based on the ASHRAE guidelines of the range 0–20 % CVRMSE and based on the results from previously developed models. When the CVRMSE is within this range, it means that the model's predictions are reasonably close to the actual data, and the model can effectively simulate the behavior of the heating and cooling systems under consideration.
- Finally, the model's performance is highly sensitive to both the training and testing durations. In summary, the proposed inverse grey-box model possesses the advantage of making short-term and long-term performance predictions that are within acceptable accuracy using a short range of training data, unlike other machine learning models such as the ANN. This is evident in this study, where even with the short range of training data, the model accuracy remained within an acceptable range in making a 10-year performance prediction. In the proposed inverse grey-box model, it is recommended to use a short range of training data (not exceeding 20 weeks) for long-term performance predictions since, beyond this range; the system exhibits a negligible performance improvement, which breaks the limitation of requiring a large range of training data for accurate model predictions over a long term in other machine learning models and provides a balance between computational resources and performance requirements.

In conclusion, a future study aims to explore the integration of these calibrated models with heat pumps for modeling, simulation, and performance evaluation of inter-seasonal consumption of surplus PV electricity in buildings.

CRediT authorship contribution statement

Fabian Eze: Writing – original draft, Visualization, Validation, Software, Methodology, Formal analysis, Data curation. **Wang-je Lee:** Resources, Data curation. **Young sub An:** Validation, Resources, Data curation. **Hongjin Joo:** Validation, Investigation. **Kyoung-ho Lee:** Supervision, Project administration, Methodology, Conceptualization. **Julius Ogola:** Supervision. **Julius Mwabora:** Supervision.

Declaration of competing interest

The authors declare that they have no known competing financial interests or personal relationships that could have appeared to influence the work reported in this paper.

Data availability

The authors are unable or have chosen not to specify which data has been used.

Acknowledgment

This work was supported by the Korea Institute of Energy Technology Evaluation Planning (KETEP) through the research project “Innovative Energy Remodeling Total Technologies for the Aging Public Buildings (No. 20202020800360)” and the Partnership for

Skills in Applied Sciences Engineering and Technology – Regional Scholarship and Innovation Fund (PASET-RSIF) by International Center of Insect Physiology and Ecology (ICIPE).

Appendix

This appendix provides more insight into the methodology for obtaining the inverse model in this study considering the given nodes in Fig. 6. More detailed mathematical description of the intermediate steps leading to the derivation of Equations (7) and (8) is presented. The equations (A- 12) and (A- 15) correspond to equations (7) and (8).

$$\text{For Node } \overline{T}_w \; 0 = \dot{Q}_w + \frac{T_g - \overline{T}_w}{R_{wg}} \tag{A- 1}$$

Where $\overline{T}_w = \frac{T_{in}+T_{out}}{2}$ and $\dot{Q}_w = \dot{m}_w c_{pw} (T_{in} - T_{out})$.

$$\text{For node } T_g : C_g \frac{dT_g}{dt} = \frac{\overline{T}_w - T_g}{R_{wg}} + \frac{T_{soil} - T_g}{R_{gs}} \tag{A- 2}$$

$$\text{For node } T_{soil} : C_{soil} \frac{dT_{soil}}{dt} = \frac{T_g - T_{soil}}{R_{gs}} + \frac{T_a - T_{soil}}{R_{as}} + \frac{T_G - T_{soil}}{R_{sG}} \tag{A- 3}$$

Substituting for $\dot{Q}_w$ in equation (A-1) and rearranging,

$$\frac{\overline{T}_w - T_g}{R_{wg}} = \dot{m}_w c_{pw} T_{in} - \dot{m}_w c_{pw} T_{out} \tag{A- 4}$$

Substitute for $\overline{T}_w$ in equation (A- 4) and rearranging,

$$\frac{1}{2R_{wg}} T_{in} + \frac{1}{2R_{wg}} T_{out} - \frac{1}{R_{wg}} T_g = \dot{m}_w c_{pw} T_{in} - \dot{m}_w c_{pw} T_{out} \tag{A- 5}$$

$$T_g = \left(0.5 - R_{wg} \dot{m}_w c_{pw}\right) T_{in} + \left(0.5 + R_{wg} \dot{m}_w c_{pw}\right) T_{out} = N_1 T_{in} + N_2 T_{out} \tag{A- 6}$$

Where $N_1 = 0.5 - R_{wg} \dot{m}_w c_{pw}$ and $N_2 = 0.5 + R_{wg} \dot{m}_w c_{pw}$.

Substituting for $\overline{T}_w$ in equation (A- 2)

$$C_g \frac{dT_g}{dt} = \frac{1}{2R_{wg}} T_{in} + \frac{1}{2R_{wg}} T_{out} - \frac{1}{R_{wg}} T_g + \frac{1}{R_{wg}} T_{soil} - \frac{1}{R_{gs}} T_g \tag{A- 7}$$

$$C_g \frac{dT_g}{dt} = \frac{1}{2R_{wg}} T_{in} + \frac{1}{2R_{wg}} T_{out} + \frac{1}{R_{gs}} T_{soil} - \left(\frac{1}{R_{wg}} + \frac{1}{R_{gs}}\right) T_g \tag{A- 8}$$

Substituting T_g in equation (A- 8) we have,

$$C_g \frac{d\left(N_1 T_{in} + N_2 T_{out}\right)}{dt} = \frac{1}{2R_{wg}} T_{in} + \frac{1}{2R_{wg}} T_{out} + \frac{1}{R_{gs}} T_{soil} - \left(\frac{1}{R_{wg}} + \frac{1}{R_{gs}}\right) \left(N_1 T_{in} + N_2 T_{out}\right) \tag{A- 9}$$

Since constant temperature of fluid is supplied during charging or discharging, $\frac{dT_{in}}{dt} = 0$ hence;

$$N_2 C_g \frac{dT_{out}}{dt} = \frac{1}{2R_{wg}} T_{in} + \frac{1}{2R_{wg}} T_{out} + \frac{1}{R_{gs}} T_{soil} - \left[\frac{N_1}{R_{wg}} T_{in} + \frac{N_2}{R_{wg}} T_{out} + \frac{N_1}{R_{gs}} T_{in} + \frac{N_2}{R_{gs}} T_{out}\right] \tag{A- 10}$$

$$C_g \frac{dT_{out}}{dt} = \frac{1}{2N_2 R_{wg}} T_{in} + \frac{1}{2N_2 R_{wg}} T_{out} + \frac{1}{N_2 R_{gs}} T_{soil} - \left[\frac{N_1}{N_2 R_{wg}} T_{in} + \frac{1}{R_{wg}} T_{out} + \frac{N_1}{N_2 R_{gs}} T_{in} + \frac{1}{R_{gs}} T_{out}\right] \tag{A- 11}$$

Substituting $N_1 = 0.5 - R_{wg} \dot{m}_w c_{pw}$ and $N_2 = 0.5 + R_{wg} \dot{m}_w c_{pw}$ in equation (A- 11) we have:

$$C_g \frac{dT_{out}}{dt} = \left(\frac{1}{R_{wg} + 2R_{wg}^2 \dot{m}_w c_{pw}} - \frac{0.5 - R_{wg}\dot{m}_w c_{pw}}{0.5R_{wg} + R_{wg}^2 \dot{m}_w c_{pw}} - \frac{0.5 - R_{wg}\dot{m}_w c_{pw}}{0.5R_{gs} + R_{gs}R_{wg}\dot{m}_w c_{pw}} \right) T_{in} + \left(\frac{1}{R_{wg} + 2R_{wg}^2 \dot{m}_w c_{pw}} - \frac{1}{R_{wg}} - \frac{1}{R_{gs}} \right) T_{out} + \left(\frac{1}{0.5R_{gs} + R_{gs}R_{wg}\dot{m}_w c_{pw}} \right) T_{soil} - C_{grout} \left(\frac{0.5 - R_{wg}\dot{m}_w c_{pw}}{0.5 + R_{wg}\dot{m}_w c_{pw}} \right) \frac{dT_{in}}{dt} \pm z \quad \text{(A- 12)}$$

Now rearranging equation (A- 3), we have:
Substituting for T_g, we have:

$$C_{soil} \frac{dT_{soil}}{dt} = \frac{1}{R_{gs}} T_g - \left(\frac{1}{R_{gs}} + \frac{1}{R_{as}} + \frac{1}{R_{sG}} \right) T_{soil} + \frac{1}{R_{as}} T_a + \frac{1}{R_{sG}} T_G \quad \text{(A- 13)}$$

$$C_{soil} \frac{dT_{soil}}{dt} = \frac{1}{R_{gs}} \left(N_1 T_{in} + N_2 T_{out} \right) - \left(\frac{1}{R_{gs}} + \frac{1}{R_{as}} + \frac{1}{R_{sG}} \right) T_{soil} + \frac{1}{R_{as}} T_a + \frac{1}{R_{sG}} T_G \quad \text{(A- 14)}$$

Substituting $N_1 = 0.5 - R_{wg}\dot{m}_w c_{pw}$ and $N_2 = 0.5 + R_{wg}\dot{m}_w c_{pw}$ we have:

$$C_{soil} \frac{dT_{soil}}{dt} = \left(\frac{0.5 - R_{wg}\dot{m}_w c_{pw}}{R_{gs}} \right) T_{in} + \left(\frac{0.5 + R_{wg}\dot{m}_w c_{pw}}{R_{gs}} \right) T_{out} - \left(\frac{R_{as}R_{sG} + R_{gs}R_{sG} + R_{gs}R_{as}}{R_{gs}R_{as}R_{sG}} \right) T_{soil} + \left(\frac{1}{R_{as}} \right) T_a + \left(\frac{1}{R_{sG}} \right) T_G \pm y \quad \text{(A- 15)}$$

References

[1] B.-K. Jeon, E.-J. Kim, Y. Shin, K.-H. Lee, Learning-based predictive building energy model using weather forecasts for optimal control of domestic energy systems, Sustainability 11 (2018) 147, https://doi.org/10.3390/su11010147.
[2] F. Eze, J. Ogola, R. Kivindu, M. Egbo, C. Obi, Technical and economic feasibility assessment of hybrid renewable energy system at Kenyan institutional building: a case study, Sustain. Energy Technol. Assessments 51 (2022) 101939, https://doi.org/10.1016/j.seta.2021.101939.
[3] A. Lyden, C.S. Brown, I. Kolo, G. Falcone, D. Friedrich, Seasonal thermal energy storage in smart energy systems: district-level applications and modelling approaches, Renew. Sustain. Energy Rev. 167 (2022) 112760, https://doi.org/10.1016/j.rser.2022.112760.
[4] L.F. Cabeza, V. Palomba, Introduction to thermal energy storage and technologies definition, in: L.F. Cabeza (Ed.), Encycl. Energy Storage, Elsevier, Oxford, 2022, pp. 329–337, https://doi.org/10.1016/B978-0-12-819723-3.00036-6.
[5] C.A. Cruickshank, C. Baldwin, Sensible thermal energy storage: diurnal and seasonal. Storing Energy, Elsevier, 2022, pp. 419–441, https://doi.org/10.1016/B978-0-12-824510-1.00018-0.
[6] Q. Chen, Z. Kuang, X. Liu, T. Zhang, Energy storage to solve the diurnal, weekly, and seasonal mismatch and achieve zero-carbon electricity consumption in buildings, Appl. Energy 312 (2022) 118744, https://doi.org/10.1016/j.apenergy.2022.118744.
[7] H. Mahon, D. O'Connor, D. Friedrich, B. Hughes, A review of thermal energy storage technologies for seasonal loops, Energy 239 (2022) 122207, https://doi.org/10.1016/j.energy.2021.122207.
[8] W. Hua, X. Lv, X. Zhang, Z. Ji, J. Zhu, Research progress of seasonal thermal energy storage technology based on supercooled phase change materials, J. Energy Storage 67 (2023) 107378, https://doi.org/10.1016/j.est.2023.107378.
[9] C. Naranjo-Mendoza, M.A. Oyinlola, A.J. Wright, R.M. Greenough, Experimental study of a domestic solar-assisted ground source heat pump with seasonal underground thermal energy storage through shallow boreholes, Appl. Therm. Eng. 162 (2019) 114218, https://doi.org/10.1016/j.applthermaleng.2019.114218.
[10] A. Lyden, C.S. Brown, I. Kolo, G. Falcone, D. Friedrich, Seasonal thermal energy storage in smart energy systems: district-level applications and modelling approaches, Renew. Sustain. Energy Rev. 167 (2022) 112760, https://doi.org/10.1016/j.rser.2022.112760.
[11] K. Kim, J. Kim, Y. Nam, E. Lee, E. Kang, E. Entchev, Analysis of heat exchange rate for low-depth modular ground heat exchanger through real-scale experiment, Energies 14 (2021) 1893, https://doi.org/10.3390/en14071893.
[12] M. Zhang, X. Liu, K. Biswas, J. Warner, A three-dimensional numerical investigation of a novel shallow bore ground heat exchanger integrated with phase change material, Appl. Therm. Eng. 162 (2019) 114297, https://doi.org/10.1016/j.applthermaleng.2019.114297.
[13] H. Mahon, D. O'Connor, D. Friedrich, B. Hughes, A review of thermal energy storage technologies for seasonal loops, Energy 239 (2022) 122207, https://doi.org/10.1016/j.energy.2021.122207.
[14] C. Zhang, Z. Guo, Y. Liu, X. Cong, D. Peng, A review on thermal response test of ground-coupled heat pump systems, Renew. Sustain. Energy Rev. 40 (2014) 851–867, https://doi.org/10.1016/j.rser.2014.08.018.
[15] T. Başer, J.S. McCartney, Transient evaluation of a soil-borehole thermal energy storage system, Renew. Energy 147 (2020) 2582–2598, https://doi.org/10.1016/j.renene.2018.11.012.
[16] A. Gultekin, M. Aydin, A. Sisman, Thermal performance analysis of multiple borehole heat exchangers, Energy Convers. Manag. 122 (2016) 544–551, https://doi.org/10.1016/j.enconman.2016.05.086.
[17] M. Abualqumboz, D. Rodley, Mathematical modelling of smart solar heating system with the deployment of borehole thermal energy storage to increase renewable heat share in Dundee, UK, Energy Proc. 151 (2018) 37–46, https://doi.org/10.1016/j.egypro.2018.09.024.
[18] ashrae-hvac-2001-fundamentals-handbook.(pdf n.d).
[19] J. Braun, N. Chaturvedi, An inverse gray-box model for transient building load prediction, HVAC R Res. 8 (2002) 73–99, https://doi.org/10.1080/10789669.2002.10391290.
[20] TRNSYS - Official Website n.d. https://sel.me.wisc.edu/trnsys/features/features.html (accessed February 22, 2024).
[21] EnergyPlus n.d. https://energyplus.net/(accessed February 22, 2024).
[22] I.R. Maestre, F.J. González Gallero, P. Álvarez Gómez, J.D. Mena Baladés, Performance assessment of a simplified hybrid model for a vertical ground heat exchanger, Energy Build. 66 (2013) 437–444, https://doi.org/10.1016/j.enbuild.2013.07.041.
[23] I.R. Maestre, F.J.G. Gallero, P.Á. Gómez, L. Pérez-Lombard, A new RC and g-function hybrid model to simulate vertical ground heat exchangers, Renew. Energy 78 (2015) 631–642, https://doi.org/10.1016/j.renene.2015.01.045.

[24] S. Tu, X. Zhang, X. Zhou, A revised thermal resistance and capacity model for the ground heat exchanger under freezing soil conditions and thermal performance analysis, Procedia Eng. 205 (2017) 19–26, https://doi.org/10.1016/j.proeng.2017.09.929.
[25] J. Kim, Y. Nam, Development of the performance prediction equation for a modular ground heat exchanger, Energies 13 (2020) 6005, https://doi.org/10.3390/en13226005.
[26] D. Lee, R. Ooka, S. Ikeda, W. Choi, Y. Kwak, Model predictive control of building energy systems with thermal energy storage in response to occupancy variations and time-variant electricity prices, Energy Build. 225 (2020) 110291, https://doi.org/10.1016/j.enbuild.2020.110291.
[27] G. Ren, A. Chuttar, D. Banerjee, Exploring efficacy of machine learning (artificial neural networks) for enhancing reliability of thermal energy storage platforms utilizing phase change materials, Int. J. Heat Mass Tran. 189 (2022) 122628, https://doi.org/10.1016/j.ijheatmasstransfer.2022.122628.
[28] K. Amarasinghe, D. Wijayasekara, H. Carey, M. Manic, Dawei He, Wei-Peng Chen, Artificial neural networks based thermal energy storage control for buildings, in: IECON 2015 - 41st Annu. Conf. IEEE Ind. Electron. Soc., IEEE, Yokohama, 2015, pp. 5421–5426, https://doi.org/10.1109/IECON.2015.7392953.
[29] H. Liu, J. Cai, A robust gray-box modeling methodology for variable-speed direct-expansion systems with limited training data, Int. J. Refrig. 129 (2021) 128–138, https://doi.org/10.1016/j.ijrefrig.2021.05.007.
[30] M.K. Khan, F. Khan, A comparative study of white box, black box and grey box testing techniques, Int. J. Adv. Comput. Sci. Appl. 3 (2012) 12–15.
[31] E. Pintelas, I.E. Livieris, P. Pintelas, A grey-box ensemble model exploiting black-box accuracy and white-box intrinsic interpretability, Algorithms 13 (2020) 17, https://doi.org/10.3390/a13010017.
[32] Y. Li, Z. O'Neill, L. Zhang, J. Chen, P. Im, J. DeGraw, Grey-box modeling and application for building energy simulations - a critical review, Renew. Sustain. Energy Rev. 146 (2021) 111174, https://doi.org/10.1016/j.rser.2021.111174.
[33] Z. Ruan, W. Sun, Y. Yuan, H. Tan, Accurately forecasting solar radiation distribution at both spatial and temporal dimensions simultaneously with fully-convolutional deep neural network model, Renew. Sustain. Energy Rev. 184 (2023) 113528, https://doi.org/10.1016/j.rser.2023.113528.
[34] H. Shi, D. Yang, W. Wang, D. Fu, L. Gao, J. Zhang, et al., First estimation of high-resolution solar photovoltaic resource maps over China with Fengyun-4A satellite and machine learning, Renew. Sustain. Energy Rev. 184 (2023) 113549, https://doi.org/10.1016/j.rser.2023.113549.
[35] GenOpt® | Simulation Research n.d. https://simulationresearch.lbl.gov/projects/genopt (accessed February 22, 2024).
[36] M. Aydin, Y.-S. Jung, H.-I. Lee, K.-D. Kim, J.-E. Yang, Calculation of thermal conductivity and heat capacity from physical data for some representative soils of Korea, Korean J Soil Sci Fertil 45 (2012) 1–8, https://doi.org/10.7745/KJSSF.2012.45.1.001.
[37] T. Nikiforova, M. Savytskyi, K. Limam, W. Bosschaerts, R. Belarbi, Methods and results of experimental researches of thermal conductivity of soils, Energy Proc. 42 (2013) 775–783, https://doi.org/10.1016/j.egypro.2013.12.034.
[38] R. Kodešová, M. Vlasáková, M. Fér, D. Teplá, O. Jakšík, P. Neuberger, et al., Thermal properties of representative soils of the Czech Republic, Soil Water Res. 8 (2013) 141–150, https://doi.org/10.17221/33/2013-SWR.
[39] L. Laloui, A.F.R. Loria, Chapter 2 - energy geostructures, in: L. Laloui, A.F.R. Loria (Eds.), Anal. Des. Energy Geostructures, Academic Press, 2020, pp. 25–65, https://doi.org/10.1016/B978-0-12-816223-1.00002-3.
[40] ASHRAE, ASHRAE Guideline 14-2014—Measurement of Energy, Demand, and Water Savings, 2014.
[41] J.W. Thornton, D.E. Bradley, N.J. Blair, T.P. McDowell, M.J. Duffy, N.D. LaHam, et al., HVAC library mathematical reference, TESSLibs 17 (2014) 6.
[42] D. Chakraborty, H. Elzarka, Performance testing of energy models: are we using the right statistical metrics? J Build Perform Simul 11 (2018) 433–448, https://doi.org/10.1080/19401493.2017.1387607.
[43] T. Hong, C.-J. Kim, J. Jeong, J. Kim, C. Koo, K. Jeong, et al., Framework for approaching the minimum CV(RMSE) using energy simulation and optimization tool, Energy Proc. 88 (2016) 265–270, https://doi.org/10.1016/j.egypro.2016.06.157.
[44] Z. Pang, F. Niu, Z. O'Neill, Solar radiation prediction using recurrent neural network and artificial neural network: a case study with comparisons, Renew. Energy 156 (2020) 279–289, https://doi.org/10.1016/j.renene.2020.04.042.
[45] C.T. Drucker, L.W. Senger, C.T. Pacioles, Application of the weibull model to describe the kinetic behaviors of thiol decolorizers in chlorogenic acid-lysine solutions, J. Food Eng. 339 (2023) 111287, https://doi.org/10.1016/j.jfoodeng.2022.111287.
[46] C. Naranjo-Mendoza, A.J. Wright, M.A. Oyinlola, R.M. Greenough, A comparison of analytical and numerical model predictions of shallow soil temperature variation with experimental measurements, Geothermics 76 (2018) 38–49, https://doi.org/10.1016/j.geothermics.2018.06.003.
[47] T. Başer, J.S. McCartney, Transient evaluation of a soil-borehole thermal energy storage system, Renew. Energy 147 (2020) 2582–2598, https://doi.org/10.1016/j.renene.2018.11.012.
[48] L. Lamarche, Horizontal ground heat exchangers modelling, Appl. Therm. Eng. 155 (2019) 534–545, https://doi.org/10.1016/j.applthermaleng.2019.04.006.
[49] A. Najib, A. Zarrella, V. Narayanan, P. Grant, C. Harrington, A revised capacitance resistance model for large diameter shallow bore ground heat exchanger, Appl. Therm. Eng. 162 (2019) 114305, https://doi.org/10.1016/j.applthermaleng.2019.114305.
[50] Q. Miao, S. You, W. Zheng, X. Zheng, H. Zhang, Y. Wang, A grey-box dynamic model of plate heat exchangers used in an urban heating system, Energies 10 (2017) 1398, https://doi.org/10.3390/en10091398.
[51] D. Zhang, P. Gao, Y. Zhou, Y. Wang, G. Zhou, An experimental and numerical investigation on temperature profile of underground soil in the process of heat storage, Renew. Energy 148 (2020) 1–21, https://doi.org/10.1016/j.renene.2019.11.123.
[52] S.-J. Cao, X.-R. Kong, Y. Deng, W. Zhang, L. Yang, Z.-P. Ye, Investigation on thermal performance of steel heat exchanger for ground source heat pump systems using full-scale experiments and numerical simulations, Appl. Therm. Eng. 115 (2017) 91–98, https://doi.org/10.1016/j.applthermaleng.2016.12.098.
[53] J. Luo, J. Rohn, M. Bayer, A. Priess, W. Xiang, Analysis on performance of borehole heat exchanger in a layered subsurface, Appl. Energy 123 (2014) 55–65, https://doi.org/10.1016/j.apenergy.2014.02.044.
[54] COMSOL - Software for Multiphysics Simulation n.d. https://www.comsol.com/(accessed February 22, 2024).